

Published in final edited form as:

Biochemistry. 2010 September 28; 49(38): 8398–8414. doi:10.1021/bi100698n.

CHARACTERIZATION OF THE N-ACETYL- α -D-GLUCOSAMINYL L-MALATE SYNTHASE (BshA) AND DEACETYLASE (BshB) FUNCTIONS FOR BACILLITHIOL BIOSYNTHESIS IN *Bacillus anthracis*^{†,‡}

Derek Parsonage^{§,||}, Gerald L. Newton^{⊥,||}, Robert C. Holder[#], Bret D. Wallace^Δ, Carleitta Paige^{§,@}, Chris J. Hamilton[§], Patricia C. Dos Santos[&], Matthew R. Redinbo^Δ, Sean D. Reid[#], and Al Claiborne^{*,§}

Center for Structural Biology and Department of Microbiology and Immunology, Wake Forest University School of Medicine, Winston-Salem, North Carolina 27157, Departments of Chemistry and Biochemistry and Biophysics, University of North Carolina at Chapel Hill, Chapel Hill, North Carolina 27599-3290, Department of Chemistry, Wake Forest University, Winston-Salem, North Carolina 27109, School of Chemical Sciences and Pharmacy, University of East Anglia, Norwich NR4 7TJ, England, and Department of Chemistry and Biochemistry, University of California, San Diego, La Jolla, California 92093-0314

Abstract

Bacillithiol (Cys-GlcN-malate, BSH) has recently been identified as a novel low-molecular-weight thiol in *Bacillus anthracis*, *Staphylococcus aureus*, and several other Gram-positive bacteria lacking glutathione and mycothiol. We have now characterized the first two enzymes for the BSH biosynthetic pathway in *B. anthracis*, which combine to produce α -D-glucosaminyl L-malate (GlcN-malate) from UDP-GlcNAc and L-malate. The structure of the GlcNAc-malate intermediate has been determined, as have the kinetic parameters for the *Ba*BshA glycosyltransferase (\rightarrow GlcNAc-malate) and the *Ba*BshB deacetylase (\rightarrow GlcN-malate). BSH is one of only two natural products reported to contain a malyl glycoside, and the crystal structure of the *Ba*BshA-UDP-malate ternary complex, determined in this work at 3.3 Å resolution, identifies several active-site interactions important for the specific recognition of L-malate, but not other α -hydroxyacids, as acceptor substrate. In sharp contrast to the structures reported for the GlcNAc—1-D-*myo*-inositol-3-phosphate synthase (MshA) apo and ternary complex forms, there is no major conformational change observed in the structures of the corresponding *Ba*BshA forms. A mutant strain of *B. anthracis* deficient in the BshA glycosyltransferase fails to produce BSH, as predicted.

[†]This work was supported by National Institutes of Health (NIH) Grants GM-35394 (A.C.), AI-78924 (M.R.R.), and AI-72133 (G.L.N.; Robert C. Fahey, Principal Investigator).

[‡]Coordinates have been deposited with the Protein Data Bank under the file name 3MBO.

*To whom correspondence should be addressed. Tel.: (336) 716-3914; Fax: (336) 777-3242 alc@csb.wfu.edu.

[§]Center for Structural Biology.

^{||}These authors contributed equally to this work.

[⊥]University of California, San Diego.

[#]Department of Microbiology and Immunology.

^ΔUniversity of North Carolina at Chapel Hill.

[@]Present address: Department of Natural Sciences, Virginia Union University, Richmond, VA 23220.

[§]University of East Anglia.

[&]Wake Forest University.

SUPPORTING INFORMATION AVAILABLE

Figures S1 and S2, depicting preparative-scale production and NMR characterization of GlcNAc-malate, Figure S3, providing reciprocal plots of *Ba*BshA activity, and Tables S1 and S2, providing the primer sequences used in the study and describing the acceptor substrate specificity for *Ba*BshA. This material is available free of charge via the Internet at <http://pubs.acs.org>.

This *B. anthracis* *bshA* locus (BA1558) has been identified in a transposon site hybridization study as required for growth, sporulation, or germination, suggesting that the biosynthesis of BSH could represent a target for development of novel antimicrobials with broad spectrum activity against Gram-positive pathogens like *B. anthracis*. The metabolites that function in thiol redox buffering and homeostasis in *Bacillus* are not well understood, and we present a composite picture based on this and other recent work.

In his recent review on the management of oxidative stress in *Bacillus*, Zuber (1) concludes that the metabolites that function in redox buffering and thiol homeostasis, and their influence on the oxidative stress response, are not well understood. Earlier work from this laboratory (2) demonstrated that CoASH provided the major low-molecular weight thiol redox buffer in *Bacillus anthracis*, replacing GSH as had previously been demonstrated for *Staphylococcus aureus* (3). The likelihood that CoASH plays an important functional role in redox buffering and thiol homeostasis is strengthened by the demonstration that both *B. anthracis* (4) and *S. aureus* (3,5-7) have NAD(P)H-dependent coenzyme A-disulfide reductases (CoADRs).¹ We have also shown that the type III pantothenate kinase, which is unusual in its insensitivity to feedback inhibition by CoASH (2), is essential for growth of *B. anthracis* (8). CoADR, the chimeric CoADR-RHD protein (9), and the type III pantothenate kinase represent three well-characterized adaptations to the CoASH-based redox buffer system for this Gram-positive pathogen.

A new unknown thiol, originally referred to as U12, was also identified in the *B. anthracis* extract (2); a mass of 398 Da was reported for U12-SH. By combining analytical chemical approaches with mass spectrometry and NMR, the structure of U12 has been determined to be *N*-cysteinyl- α -D-glucosaminyl L-malate, and U12 has been renamed bacillithiol [BSH (10)]. BSH is present at intracellular concentrations of 0.1-0.35 mM² in a number of *Bacillus* species, including *B. anthracis*, *Bacillus subtilis*, and *Bacillus megaterium*, as well as in *S. aureus*. While none of the four *B. subtilis* strains represented in the NCBI database have orthologs of CoADR or any of its isoforms (9), *B. anthracis*, *B. megaterium* (11), and *S. aureus* (3) maintain both CoASH and BSH redox buffer systems, in the absence of GSH. Pöther et al. (12), in a recent study with *S. aureus* demonstrating that the majority of reversible protein thiol oxidations observed during treatment of cells with diamide are based on *S*-thiolations with Cys rather than protein disulfide formation, have concluded that Cys also functions as an important thiol redox buffer in *S. aureus*.

In an initial study of the biosynthesis and functions of BSH (13), we have demonstrated that the *B. subtilis* YpjH protein (*BsuBshA*), the enzyme orthologous to *B. anthracis* ORF BA1558, catalyzes the synthesis of *N*-acetyl- α -D-glucosaminyl L-malate (GlcNAc-malate) from UDP-GlcNAc and L-malate; the product structure has been confirmed by mass spectrometry (10,13). We have also demonstrated that the BA1557 gene product (*BaBshB*) catalyzes the deacetylation of GlcNAc-malate (13), providing the free 2-amino group of the GlcN moiety required for the Cys ligation step that is proposed to complete the synthesis. Deletion of the *B. subtilis* *yllA* locus, predicted to be involved in the biosynthetic pathway

¹Abbreviations: CoADR, coenzyme A-disulfide reductase; CoADR-RHD, coenzyme A-disulfide reductase isoform with a C-terminal rhodanese homology domain; BSH, bacillithiol; BshA, *N*-acetyl- α -D-glucosaminyl L-malate synthase; GlcNAc-malate, *N*-acetyl- α -D-glucosaminyl L-malate; BshB, *N*-acetyl- α -D-glucosaminyl L-malate deacetylase; GlcN-malate, α -D-glucosaminyl L-malate; MshA, *N*-acetyl- α -D-glucosaminyl 1-D-*myo*-inositol-3-phosphate synthase; Ins, *myo*-inositol; MSH, mycothiol; GT, glycosyltransferase; BcZBP, *Bacillus cereus* zinc-binding protein; MshB, *N*-acetyl- α -D-glucosaminyl 1-D-*myo*-inositol-3-phosphate deacetylase; BHI, Brain Heart Infusion; LB, Luria-Bertani; Ery^R, erythromycin-resistant; Tet^R, tetracycline-resistant; HEPES, *N*-(2-hydroxyethyl)piperazine-*N'*-2-ethanesulfonic acid; HPLC, high-performance liquid chromatography; ESP, electrospray; gCOSY, gradient correlation spectroscopy; RSmB, methylbimane derivative of thiol, RSH, from reaction with monobromobimane; Mca, mycothiol *S*-conjugate amidase; TrxR, thioredoxin reductase; Trx, thioredoxin; Grx, glutaredoxin.

²Intracellular concentrations are calculated from BSH contents ($\mu\text{mol/g}$ dry weight), using a value of 2 $\mu\text{L/mg}$ dry weight for the cell volume (Ref 2).

and initially suggested to encode this putative ligase, does eliminate BSH production; the recombinant protein, however, does not catalyze ATP-dependent BSH formation from Cys and GlcN-malate, as assayed *in vitro*.

In the absence of functional information, Ruane et al. (14) have reported the structure of the ORF BA1558 (identified in this work as *BaBshA*) apoenzyme, refined at a resolution of 3.1 Å. Although this enzyme, like the MshA glycosyltransferase that produces GlcNAc-Ins-P in the first step of mycothiol (MSH) biosynthesis (15,16), is a member of the GT-B and GT4 fold (17) and Carbohydrate-Active enZymes (18) families, respectively, structural homology searches using the MshA apoenzyme structure were unsuccessful in identification of other GT-B family members, including ORF BA1558. This indicates a major conformational difference between the two apoenzymes, despite the similarity in reactions catalyzed. Fadoulglou et al. (19) reported the crystal structure of the Zn²⁺-binding *BcZBP* protein from *Bacillus cereus*, as refined at a resolution of 1.8 Å. *BcZBP* is the enzyme orthologous to *BaBshB*, the GlcNAc-malate deacetylase, with 97% sequence identity. A recent kinetic analysis (20) with GlcNAc and several GlcNAc oligomers indicated that, although the biological function and natural substrate for *BcZBP* were unknown, the enzyme had optimal activity with (GlcNAc)₂ ($k_{\text{cat}}/K_m = 3.3 \times 10^7 \text{ M}^{-1}\text{s}^{-1}$ at 37°C). The enzyme is a member of the PIG-L superfamily represented by GlcNAc-phosphatidylinositol deacetylase (21), the MshB deacetylase (22) of the MSH biosynthetic pathway, and the mycothiol S-conjugate amidase (23). The active-site Zn²⁺ of *BcZBP* is buried at the bottom of a ca. 12 Å deep cavity on the hexamer surface, and Arg140 is prominently positioned at the entry of the cavity. Both R140A and R140E mutants exhibit k_{cat}/K_m values 0.2-0.3% that of wild-type enzyme (20). His12, Asp15, and His113 provide the protein ligands to the Zn²⁺, and Asp14 has been proposed as an acid-base catalyst in the hydrolase reaction. A model of a *BcZBP*-GlcNAc complex reveals that this substrate is considerably smaller than the volume of the cavity; a hydrophilic patch consisting of the side chains of Asp108, Asn150, and Tyr194 marks an unoccupied region proximal to the Zn²⁺. The Y194F mutant specificity constant, which is <0.1% that of wild-type (20), reflects a dominant effect on K_m . In particular, the anomeric C1-OH of GlcNAc also appears to be accommodated by a relatively large space within the cavity. For the *BcZBP* apoenzyme structure, three very mobile loops have recently been implicated in determining active-site accessibility and regulating substrate specificity (24).

Given the goal of better defining the thiol redox buffer in *B. anthracis* and characterizing potential new targets for the development of antimicrobial agents that are selective against *B. anthracis*, *S. aureus*, and other Gram-positive pathogens that rely on the BSH-based redox buffer system, we report here detailed kinetic analyses of the *BaBshA* glycosyltransferase and *BaBshB* deacetylase. The kinetic studies are interpreted in view of the ORF BA1558 and *BcZBP* crystal structures, and we also provide the structure of the *BaBshA*-UDP-malate complex, refined at a resolution of 3.3 Å, which demonstrates the absence of any major conformational change on ligand binding. In addition we show that deletion of the BAS1445 locus encoding BshA in *B. anthracis* Sterne generates a BSH-deficient strain appropriate for testing in a murine model of inhalational anthrax.

EXPERIMENTAL PROCEDURES

Bacterial Strains and Antibiotics

The *B. anthracis* Sterne 34F2 strain (pXO1⁺ pXO2⁻) used in these studies was obtained from Dr. Philip Hanna, University of Michigan Medical School. Cultures were grown and maintained in BHI broth (Difco) and on solid media containing 15 g/L of agar. For preparation of parental and mutant endospores, cultures were grown at 37°C on BHI plates containing antibiotics as appropriate. A single colony was inoculated into 3 mL of BHI broth

containing antibiotics as required, and this culture was taken as the inoculum (5%, v/v) into 75 mL of fresh modified G (sporulation) medium (25) without antibiotic, after 8-12 h of growth. After 4 days' growth at the appropriate temperature endospores were collected by centrifugation, and residual vegetative cells were killed by a 30-min incubation at 65°C. Pellets were washed 3-4 times in deionized water, and endospores were stored (in deionized water) at ambient temperature. The purity of the spore preparations was confirmed by phase-contrast microscopy, and spore titers were determined by serial dilution. *Escherichia coli* strains DB3.1 (26) and GM272 were used for the cloning and propagation of pBKJ236 and pBKJ223 (27), respectively. DB3.1(pBKJ236) was cultured and maintained in LB broth or on solid media supplemented with 250-400 µg/mL erythromycin. GM272(pBKJ223) was cultured and maintained in LB broth or on solid media supplemented with 15 µg/mL tetracycline.

Construction of *B. anthracis* Sterne Deletion Strains

In-frame deletion mutants of the genes encoding *BaBshA* (*bshA*, loci BA1558 and BAS1445 in Ames and Sterne strains, respectively), *BaBshB* (*bshB*, loci BA1557 and BAS1444, respectively), *BaCoADR* [*cdr*, loci BA1263 (4) and BAS1170, respectively] and *BaCoADR-RHD* [*cdr2*, loci BA0774 (9) and BAS0736, respectively] were constructed following the markerless gene replacement protocol (27), using the pBKJ236 and pBKJ223 plasmids. The procedure followed in this work is described in detail for the $BAS\Delta 1445$ mutant. A modified chromosomal segment containing the BAS1445 deletion was constructed by first amplifying the flanking upstream and downstream regions (>500 bp each) using primer sets BAS1445up (FWD/REV) and BAS1445down (FWD/REV), respectively (Table S1). The two amplified products were then ligated using overlap PCR with BAS1445up FWD/BAS1445down REV, and the resulting deletion fragment was TA cloned into pCR2.1 (Invitrogen) before subcloning into pBKJ236 digested with *NotI*. This plasmid, pBKJ236::BAS1445' was electroporated into methylation-deficient (*dam⁻ dcm⁻*) *E. coli* GM272. *E. coli* GM272(pBKJ236::BAS1445') (LB plus 250 µg/mL erythromycin), *E. coli* helper strain 459 (LB plus 100 µg/mL ampicillin), and *B. anthracis* Sterne were grown overnight, and aliquots (75 µL) from washed samples of each culture were mixed and spotted onto BHI agar before incubating for 48 h at room temperature. The accumulated growth was resuspended in fresh LB broth, and 150 µL of the suspension was dispensed in a "straight line" on one quadrant of a BHI agar plate supplemented with 5 µg/mL erythromycin and 80 U/mL polymyxin B. After the line was allowed to dry, cells were streaked to isolation and incubated at room temperature for 48 h. Isolated Ery^R colonies were cultured overnight, again at room temperature, before diluting 1:1000 in fresh BHI broth plus erythromycin and shifting to 37°C, a nonpermissive temperature for plasmid replication. Following this overnight incubation, integrants were isolated using the "straight line" procedure described above, but with incubation at 37°C on BHI agar plus erythromycin. A single Ery^R colony was grown out, to A₆₀₀ ca. 0.2, in 25 mL of LB plus glucose (28) at 37°C, with shaking at 100 rpm; cells were harvested by centrifugation at 4°C, resuspended and washed in ice-cold electrotransformation buffer (29), and transferred (400 µL) to a chilled 0.4-cm electrode-gap cuvette. After 10 min incubation on ice, with 5 µL of unmethylated pBKJ223 [isolated from *E. coli* GM272(pBKJ223)], cells were electroporated at 2.4 kV, 200 Ω and 25 µF. After pulsing, cells were placed back on ice, and 700 µL of ice-cold LB plus glucose was added; the mixture was transferred to a microcentrifuge tube, and cells were allowed to recover for 3 h at 30°C before plating on BHI agar plus 10 µg/mL tetracycline and incubating overnight at 37°C. Several single Tet^R colonies selected after repeatedly mixing and streaking to isolation were patched onto BHI agar plus erythromycin and BHI agar plus tetracycline and incubated overnight at 37°C. Clones with the desired Tet^R Ery^S (loss of pBKJ236) phenotype were validated by colony PCR, repurified by streaking, and patched onto BHI agar with and without tetracycline.

Clones cured of Tet^R (loss of pBKJ223) were again validated by colony PCR to confirm the BAS1445 deletion. $\Delta bshB$, Δcdr , and $\Delta cdr2$ mutants were constructed following the same protocol; the $\Delta cdr\Delta cdr2$ double mutant utilized the Δcdr strain in the initial conjugation step.

Fosfomycin Sensitivity of Wild-Type and Δbsh Strains

An active culture grown to A₆₀₀ of 0.5 (mid-log) was used to inoculate (1% v/v) 5 mL aliquots of fresh BHI broth containing fosfomycin at incremental concentrations. The wild-type Sterne strain showed robust growth (static conditions in 17 × 100 mm polystyrene tubes) at all fosfomycin concentrations (0-1,000 µg/mL). The $\Delta bshA$ mutant grew only in the control (no fosfomycin) culture and at the lowest fosfomycin concentration tested (200 µg/mL), but not at concentrations ≥400 g/mL. The $\Delta bshB$ mutant was sensitive to fosfomycin at 800 µg/mL, but not at ≤400 µg/mL.

Expression and Purification of *B. anthracis* BshA, BshB, and CysS

The codon-optimized BA1558 and BA1557 genes, encoding *BaBshA* and *BaBshB*, respectively, were synthesized by GenScript (Piscataway, NJ) and subcloned into pET28a(+) (Novagen). Both genes were expressed in *E. coli* BL21(DE3) cells using auto-induction media at 37°C (30); BshA was expressed with an N-terminal His-tag (see “Results”), while BshB had a C-terminal His-tag (-LEH₆). All steps of both purifications were carried out at 4°C. Harvested cells were disrupted using an Avestin EmulsiFlex-C5 homogenizer, and nucleic acids were removed by addition of 2% streptomycin sulfate and centrifugation (27,000g for 20 min). For BshA, the clarified extract was loaded onto a 25-mL Ni Sepharose High Performance column (GE Healthcare, Piscataway, NJ) in 50 mM sodium phosphate, pH 8.0, containing 0.3 M NaCl and 20 mM imidazole; the protein was eluted with a stepwise increase of imidazole, to 250 mM. Peak fractions were pooled and loaded onto a Q-Sepharose HP column after dialysis against 20 mM HEPES, pH 7.5, containing 50 mM NaCl. The protein was eluted with a linear 375-mL gradient of 0.05 → 1 M NaCl, and the *BaBshA* pool was dialyzed against the Q-Sepharose loading buffer before concentrating and storing in aliquots at -80°C. For *BaBshB*, the immobilized metal-ion affinity chromatography column was first converted to the Zn²⁺ form (31); the clarified extract was loaded onto the 25-mL Zn Sepharose column in 50 mM sodium phosphate, pH 8.0, containing 0.3 M NaCl and 20 mM imidazole. The protein was eluted with a stepwise increase of imidazole, to 250 mM. Peak fractions were pooled and loaded onto a Q-Sepharose HP column after dialysis against 25 mM potassium phosphate, pH 7.0. The protein was eluted with a linear 375-mL gradient of 0 → 1 M NaCl, and the purified *BaBshB* protein was dialysed against 25 mM Tris-HCl, pH 8.0, containing 50 mM NaCl, concentrated by ultrafiltration, and brought to a final concentration of 20% (v/v) glycerol before being frozen in aliquots at -80°C.

The cysteinyl-tRNA synthetase gene (*cysS*, BA0089) was amplified from genomic *B. anthracis* DNA using primers designed with *NcoI* and *XhoI* linkers that allowed cloning into pET28a. The recombinant C-terminal His-tagged CysS protein was expressed in *E. coli* BL21(DE3); cultures grown to mid-log phase in LB plus kanamycin at 37°C were induced with lactose for 3 h. Harvested cells were resuspended in 1.5 volumes of degassed 50 mM Tris-HCl, pH 8.0, containing 0.5 M NaCl, and were lysed with a French press. The extract was clarified by centrifugation and applied to a Ni²⁺-charged metal-ion affinity column (GE Healthcare) equilibrated with the lysis buffer; the column was washed with this buffer containing 20 mM imidazole before the recombinant CysS protein was eluted with 100 mM imidazole. Pooled fractions were diluted with 5 volumes of lysis buffer and loaded onto a HiTrap Q XL column (GE Healthcare); the column was washed with the lysis buffer before eluting the protein with a linear 50-mL gradient of 0 → 1 M NaCl. The cysteine adenylation

activity of *B. anthracis* CysS was assayed using the ATP-³²PP₁ exchange reaction in the presence of 50 μM Cys (32).

Enzymatic Synthesis of GlcNAc-malate

GlcNAc-malate required for kinetic analysis of *BaBshB* was produced on a preparative scale by incubating 0.5 mg *BaBshA* at 37°C with 50 μmol each of UDP-GlcNAc and L-malate (substrates purchased from Sigma) in 5 mL of 25 mM HEPES, pH 7.5, containing 100 mM NaCl, 10 mM MgCl₂, and 1 mM 2-mercaptoethanol. The reaction was sampled at indicated times; samples were processed as described by Newton et al. (15) for identification of the MshA-catalyzed reaction products (using unlabeled substrates) and were analyzed by HPLC with A₂₆₀ detection for UDP-GlcNAc and UDP. The conversion of UDP-GlcNAc → UDP was complete in 2 h. The GlcNAc-malate product (50 μmol, ca. 15 mg) was processed for preparative HPLC purification by 1) adding 1 volume of acetonitrile to the reaction mixture and incubating at 60°C for 15 min, 2) clarifying by centrifugation, and 3) adjusting the supernatant pH→3 with trifluoroacetic acid after reducing the volume to 2 mL in a SpeedVac. A Vydac 218TP1022 (1 × 25 cm) reversed-phase preparative column was used with a linear gradient from 0→20% methanol in 0.1% trifluoroacetic acid, over 40 min (flow rate of 5 mL/min), with online detection by mass spectrometry. Fractions containing GlcNAc-malate (ESP, *m/z* 336) were combined, and the separation was repeated to obtain the purified product, which was adjusted to pH 6 with NaOH and lyophilized.

Synthetic GlcNAc-malate was maintained at -70°C in H₂O at a concentration of 80 mM and contained ca. 1 equiv sodium trifluoroacetate from the HPLC solvent. The sodium trifluoroacetate content was determined in the quantitative pH titration described above. In addition, the disodium GlcNAc-malate content determined by the *BaBshB*—Accu-Tag method (see below) accounts for ca. 50% of the total mass of the lyophilized material. ¹H- and gCOSY NMR spectra were recorded on a Jeol ECA500 at 500 MHz and were referenced to residual solvent (HDO) at 4.8 ppm. The ¹H NMR of GlcNAc-malate in D₂O (trifluoroacetate is not observable) confirmed the absence of other organic impurities. ¹³C spectra were collected on a Varian X500 (125 MHz) equipped with an XSENS cold probe. All spectra were collected at 23°C. High resolution mass spectrometry analysis was provided by the UCSD Chemistry and Biochemistry Mass Spectrometry Facility using a Thermo Scientific LTQ Orbitrap XL mass spectrometer operating in positive ion mode ESP ionization.

BaBshA and BaBshB Kinetic Parameters

The kinetic properties of *BaBshA* were first analyzed from initial rates of UDP-GlcNAc → UDP conversion, using the A₂₆₀-based HPLC assay described above (15) for monitoring GlcNAc-malate synthesis. Initial rates were determined over a range of UDP-GlcNAc concentrations (0→25 mM) at a fixed concentration of 2 mM L-malate (ca. 15 × K_m, see “Results”); for each individual assay at 37°C [in 25 mM HEPES, pH 7.5, containing 100 mM NaCl, 10 mM MgCl₂, and 1 mM 2-mercaptoethanol], the reaction was sampled four times in order to establish the observed rate of UDP formation. Similarly, initial rates were measured over a series of L-malate concentrations (0→3.2 mM) at a fixed concentration of 3 mM UDP-GlcNAc (ca. 5 × K_m). Results representing the mean of triplicate determinations were fit to the Michaelis-Menten equation [equation 1 (33)] where V_{max} is the apparent maximal velocity, A is the concentration of the varied substrate, and K_A is the Michaelis constant (apparent) for substrate A.

$$v = V_{\max} \cdot A / (K_A + A) \quad (\text{Eq. 1})$$

Data described with this single variable equation were analyzed using KaleidaGraph.

In order to analyze the steady-state kinetic mechanism with several fixed concentrations of UDP-GlcNAc and L-malate, respectively, the continuous spectrophotometric assay for glycosyltransferases (34) was adapted, using a 96-well format with a POLARstar OPTIMA (BMG LABTECH) microplate reader. For each assay at 37°C, 30 ng of *BaBshA* was incubated in 25 mM HEPES, pH 7.5, containing 50 mM KCl, 10 mM MgCl₂, 7.5 U pyruvate kinase and 15 U lactate dehydrogenase (both enzymes purchased from Sigma), 0.8 mM phosphoenolpyruvate, and 0.15 mM NADH in a final volume of 200 μL. The concentration of L-malate was varied over the range 0.08-1.2 mM at fixed concentrations of 0.1-1.5 mM UDP-GlcNAc. Reactions were initiated by addition of enzyme and were performed in duplicate. These results (for varying [L-malate]) were fit to the reciprocal form of the velocity equation for a rapid equilibrium random system [equation 2 (33)], using GraFit version 5.

$$\frac{1}{v} = \frac{\alpha K_{\text{Acc}}}{V_{\text{max}}} \left(1 + \frac{K_{\text{Don}}}{[\text{Don}]} \right) \left(\frac{1}{[\text{Acc}]} \right) + \frac{1}{V_{\text{max}}} \left(1 + \frac{\alpha K_{\text{Don}}}{[\text{Don}]} \right) \quad (\text{Eq. 2})$$

where Don = UDP-GlcNAc and Acc = L-malate. α is a factor representing the effect each substrate has on the binding of the second substrate. Controls showed that the omission of 2-mercaptoethanol and substitution of 50 mM KCl for 100 mM NaCl in the coupled assay had no effect on initial velocity. In addition, any competitive UDP-GlcNAc hydrolysis reaction (measured in the absence of L-malate) was negligible.

The kinetic parameters for *BaBshB* were determined from initial rates of GlcNAc-malate → GlcN-malate conversion, using an HPLC assay for the AccQ-Tag derivative of the GlcN-malate product, as monitored by fluorescence (13,31,35). Initial rates were determined over a series of GlcNAc-malate concentrations (0→2 mM); for each assay at 37°C [in 50 mM HEPES, pH 7.5, containing 50 mM NaCl and 1 equiv of sodium trifluoroacetate per mol GlcNAc-malate], the reaction was sampled at intervals in order to establish the rate of GlcN-malate formation. Results representing the mean of triplicate determinations were fit to equation 1 as described above. Bacillithiol *S*-conjugate amidase activity was measured using the methylbimane derivative of BSH (BSmB) purified as described (10). The reaction was sampled at intervals; aliquots were processed for analysis, using an adaptation of the fluorescence-based HPLC assay for CySmB (+ GlcN-malate) product formation described previously (23). The initial rate of CySmB formation was determined by sampling the reaction four times in the presence of 320 μM BSmB.

Crystallographic Methods

After purification *BaBshA* was buffer-exchanged into 20 mM HEPES, pH 7.5, containing 150 mM NaCl plus 5 mM dithiothreitol, and concentrated to 16 mg/mL for crystallization. Crystals were obtained in 0.2 M Mg(HCO₂⁻)₂ containing 15% PEG3350 with 1 mM each of UDP and L-malate. Crystals were cryoprotected with mother liquor supplemented with 25% glycerol and flash-frozen in liquid nitrogen. *BaBshA* crystals, which appeared after 4-5 days, diffracted to 3.3 Å. Data sets were collected at SER-CAT beamline 22-BM (Advanced Photon Source, Argonne National Laboratory). Data were indexed and scaled using HKL2000 (36). Molecular replacement was performed using PHASER (37), and model refinement was carried out using the PHENIX software suite (38). The model was adjusted manually using COOT (39) as well as 2*F_o*-*F_c* and *F_o*-*F_c* electron density maps. The UDP and L-malate model and definition files were generated with PHENIX.

Analysis of Thiols from Wild-Type and Mutant Strains of *B. anthracis*

All manipulations of *B. anthracis* Sterne strains were carried out under Biosafety Level 2 conditions at Wake Forest University School of Medicine and at University of California, San Diego. The detailed methods for culture growth, sample preparation, and analysis, including the determination of thiol redox status, are given in Nicely et al. (2) and Newton et al. (10).

Bioinformatics

Sequence analyses were performed with the NCBI and PDB databases using BLASTP, and the resources of the Carbohydrate-Active enZymes database (18) were also utilized in this work. Structure superpositions and sequence alignments were performed using DALILITE (40), PyMOL (41), CLUSTALW (42), and ESPript (43), respectively. Figures of protein molecules and residues were prepared using PyMOL.

RESULTS

Proposed BSH Biosynthetic Pathway in *B. anthracis*

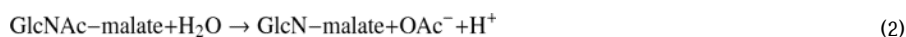
Given the structural similarity between bacillithiol and mycothiol (Figure 1) and the well-defined pathway for MSH biosynthesis in *Mycobacterium tuberculosis* and other *Actinobacteria* (44,45), three distinct enzymatic steps have been considered in the pathway for BSH biosynthesis (Figure 2). The first reaction produces GlcNAc-malate from UDP-GlcNAc and L-malate, as indicated:



We have demonstrated (13) that the *B. subtilis* YpjH gene product catalyzes the synthesis of GlcNAc-malate as given in reaction (1). In *B. anthracis* the BA1558 locus is the ortholog of *B. subtilis* *ypjH*; as shown in the preparative scale assay (Figure S1), ORF BA1558 catalyzes the production of UDP and GlcNAc-malate when incubated with UDP-GlcNAc and L-malate. Isolation of the GlcNAc-malate product from this preparative scale reaction allowed its confirmation by ¹H and ¹³C NMR (Figure S2) and high resolution mass spectrometry. The proton NMR spectra (Figure S2A) indicated that the GlcNAc-malate was pure (see “Experimental Procedures”) and contained the L-malate and D-glucosamine resonances found in bacillithiol (10). The glucosamine *N*-acetyl group is validated by the acetyl protons (singlet, 2.04 ppm) and the carbon resonances at 174.3 and 21.9 ppm (Figure S2B). The carbon 2 proton (3.9 ppm) of glucosamine (nitrogen bonded carbon) is identified in the gCOSY spectra (Figure S2A) by correlation to the anomeric proton. The anomeric proton (4.89 ppm) coupling constant (3.8 Hz) indicated this was the α -anomer of the malyl glycoside as predicted by the structure of bacillithiol. The high-resolution mass spectra of this compound gave a mass of 360.0902 for the sodium ion of GlcNAc-malate (360.0901, δ 0.3 ppm) corresponding to a formula of C₁₂H₁₉NO₁₀Na, consistent with the product of *BaBshA*. Confirmation of the novel D-glucosaminyl L-(α)-malate moiety validates the structure of bacillithiol from *Deinococcus radiodurans* (10) and shows that it is identical to bacillithiol produced in *B. anthracis*. ORF BA1558 is the BshA glycosyltransferase in *B. anthracis* and is therefore designated *BaBshA* (Figure 2).

When the structure of the *M. tuberculosis* GlcNAc-Ins deacetylase MshB [PDB entry 1Q74 (22)] was used to query the Protein Data Bank with DALILITE, the highest score ($Z = 21.6$) was observed with the Zn²⁺-binding *BcZBP* protein [PDB entry 2IXD; rmsd = 2.3 Å, 24% identity (19)] from *B. cereus*. This deacetylase is 97% identical in sequence to the *B. anthracis* ortholog, ORF BA1557. We have recently demonstrated (13) that recombinant

ORF BA1557 catalyzes the efficient deacetylation of GlcNAc-malate → GlcN-malate, as given in reaction (2):



The preparative scale reaction, using GlcNAc-malate prepared by enzymatic synthesis with *BaBshA* and purified by HPLC (see “Experimental Procedures”), allowed isolation of the GlcN-malate product, and deacetylation of the substrate was confirmed by ESP mass spectrometry. ORF BA1557 is the *BshB* GlcNAc-malate deacetylase in *B. anthracis* and is therefore designated *BaBshB*. We have now identified the enzymatic activities, *in vitro*, for the *BaBshA* glycosyltransferase and the *BaBshB* deacetylase. Thus, from UDP-GlcNAc and L-malate precursors, these enzymes combine to produce GlcN-malate, UDP, and acetate; GlcN-malate has also been identified by HPLC analysis of cell-free extracts from *B. subtilis* (13), confirming this aspect of the BSH biosynthetic pathway as presented in Figure 2 for *B. anthracis*. While we have not attempted to identify GlcNAc-malate *in vivo*, these combined results provide very strong evidence that the biosynthetic scheme presented in Figure 2 for *BshA* and *BshB* represents the intracellular process in *B. anthracis*.

These functional assignments, as confirmed experimentally, leave the enzyme(s) responsible for the proposed ATP-dependent Cys:GlcN-malate ligase reaction (Figure 2) unidentified. The *mshC* gene product in *M. tuberculosis* is a second cysteinyl-tRNA synthetase isoform that differs from the functional CysS enzyme primarily through the absence of a 76-residue C-terminal extension that is responsible for recognition and specific binding of the tRNA^{Cys} anticodon (46,47); the Cys:GlcN-Ins ligase catalyzes the ATP-dependent formation of the amide linkage in the ultimate MSH product (+ AMP + PP_i). BLASTP analysis of the *B. anthracis* genome, however, fails to identify any second CysS isoform, and the ORF BA0089 (annotated as cysteinyl-tRNA synthetase) protein as expressed is active in the standard tRNA synthetase assay. Although deletion of the *B. subtilis yllA* locus eliminates BSH production with a concomitant increase in intracellular GlcN-malate (the *BshB* product), the recombinant *B. subtilis YllA* and *S. aureus* CysS proteins both fail to catalyze ATP-dependent production of BSH from Cys and GlcN-malate in an *in vitro* assay (13).

Genetic Analysis of *bshA* and *bshB* Functions in *B. anthracis*

Passalacqua et al. (48) have recently demonstrated that the seven genes corresponding to BA1554-BA1560 (Ames strain) are transcribed as a single mRNA unit in *B. anthracis* Sterne (BAS1441-BAS1447); this experimental result is consistent with results obtained earlier with the operon prediction algorithm developed by Bergman et al. (49). Given the involvement of both BSH and CoASH in the *B. anthracis* thiol redox buffer (2,10), we note that the BA1562-BA1564 loci (*panBCD*) encoding three key enzymes in the synthesis of the CoASH precursor pantothenate (50) are separated by a single ORF from the *bsh* operon and have been demonstrated to be cotranscribed together with BA1565 in a second tetracistronic operon (48). In the event that candidate *bshC* loci might be clustered within the *bsh* operon, we analyzed the seven protein products for structural homologs of known function, using the PDB and NCBI databases. Table 1 summarizes details of the structural and functional annotations for each of the ORFs in the *bsh* and *pan* operons. Although there may be a functional linkage between BSH production and methylglyoxal synthase [ORF BA1556 (51)] activity (see “Discussion”), we find no evidence for candidate *bshC* loci in either *bsh* or *pan* operons in *B. anthracis*.

In contrast to the soil bacterium *B. subtilis*, which lacks the CoASH thiol redox buffer (9), the redundancy provided by the CoASH and BSH redox buffers in *B. anthracis* and *S. aureus* may provide these two pathogens with some advantage in virulence and/or survival,

given the hostile environment posed by host defense mechanisms (52,53). The results described above predict that individual deletions of the *bshA* and *bshB* genes in *B. anthracis* Sterne (loci BAS1445 and BAS1444, respectively) will disrupt the BSH biosynthetic pathway at the points of GlcNAc-malate and GlcN-malate precursor production, respectively. The two mutants were prepared using the markerless deletion method developed by Janes and Stibitz (27) and were analyzed for low-molecular-weight thiol content in parallel with wild-type *B. anthracis* Sterne and deletion mutants lacking the *cdr* and *cdr2* genes that encode *BaCoADR* (4) and the chimeric CoADR-RHD protein (9). The major conclusions from the analytical data presented in Table 2 are as follows: 1) deletion of the *bshA* locus eliminates BSH production, 2) deletion of the *bshB* locus does not eliminate BSH production but reduces it by 30% relative to wild-type, 3) BSH redox status (BSH/BSSB) strongly favors the reduced thiol in vegetative *B. anthracis* cells, and this is not affected by deletions of the *cdr* and/or *cdr2* loci, 4) the value for CoASH is higher (1.9 ± 0.4 $\mu\text{mol/g}$ dry residual weight) than that reported previously [0.87 ± 0.11 $\mu\text{mol/g}$ (2)]; this is attributed to the different wild-type strains used in the two analyses, 5) Cys is a major low-molecular weight thiol, consistent with the recent report of Pöther et al. (12), for *S. aureus*, and 6) thiosulfate ($\text{S}=\text{SO}_3^{2-}$), a principal source of sulfur for aerobic bacteria (54) and donor substrate for the sulfurtransferase rhodanese (55), is a major inorganic sulfur compound in *B. anthracis*.

In *B. subtilis* the primary fosfomycin resistance determinant FosB functions as a thiol-dependent *S*-transferase that produces a thioether conjugate from the thiol and the antibiotic; until very recently, however, the enzyme had only been demonstrated to work quite poorly *in vitro* (56), with Cys as thiol substrate. Using a zone of inhibition assay we have recently demonstrated (13) that a *B. subtilis* mutant deficient in BSH is as sensitive to fosfomycin as a *fosB* mutant, leading to the conclusion that FosB is a BSH *S*-transferase. We tested the sensitivity of wild-type and $\Delta bshA$ mutant strains of *B. anthracis* to fosfomycin in liquid culture. While the wild-type strain grew well at 1,000 $\mu\text{g/mL}$ fosfomycin, the *bshA* mutant did not grow at fosfomycin concentrations ≥ 400 $\mu\text{g/mL}$. *B. anthracis* ORF BA4109 is annotated as the FosB protein, and we propose that this enzyme requires BSH as a cofactor for conjugation in the detoxification of fosfomycin (Scheme 1).

Our results with the $\Delta bshB$ mutant clearly indicate that other protein(s) capable of recognizing and deacetylating GlcNAc-malate are expressed in *B. anthracis*. Fadouloglou et al., in their earlier structural analysis of *BcZBP* (19), had identified ORF *Bc3461* as a *BcZBP* paralog; more recently, this analysis was extended (24) with the identification of the BA630 (*BaBshB*), BA425 (ORF BA3524), and BA758 (ORF BA3888) orthologs in the *B. anthracis* genome (Figure 3). ORF *Bc3461* has now been expressed and characterized (20); when assayed in parallel with *BcZBP*, the enzyme shows a preference for $(\text{GlcNAc})_2$ and $(\text{GlcNAc})_3$ as deacetylase substrates. $k_{\text{cat}}/K_m(\text{GlcNAc})_2 = 5.6 \times 10^6 \text{ M}^{-1}\text{s}^{-1}$, or ca. 20% that of *BcZBP*. While its biological role is unclear, ORF *Bc3461* has potent deacetylase activity. Figure 3 gives a structure-based sequence alignment for *BcZBP*, *BaBshB*, ORF BA3888, ORF BA3524, and ORF *Bc3461*. While BA3888 and BA3524 have limited sequence similarity to *BcZBP* (26-28% identity), the latter protein is 95% identical in sequence to *Bc3461*; all three conserve the three Zn^{2+} protein ligands identified in *BcZBP* as well as the proposed active-site base and charge-relay dyad (His110/Asp112). These conserved features identify these as Zn^{2+} -dependent hydrolases³; Figure 3 also identifies a series of conserved insertions and deletions that distinguish the true BshB deacetylases *BcZBP* and *BaBshB* from the three paralogs. These include a 10-residue insert *II* (relative to *BcZBP*) after Ser45,

³Purification of the recombinant *BcZBP* protein employed Ni-NTA chromatography and resulted in Zn^{2+} -containing *BcZBP* crystals (Ref 19), as analyzed by both X-ray fluorescence and X-ray diffraction. Similar purification of the MshB protein (Ref 31), however, yielded a preparation with no Zn^{2+} and 0.82 mol Ni^{2+} per subunit.

two small inserts (1-2 residues) following *BcZBP* Lys82 and Asp108, and two deletions *D1* and *D2* of 4-6 residues following Ile129 and Phe205, respectively. The *I1* insert falls within the hypermobile *BcZBP* active-site loop *L46*, and the *D1* deletion falls within the *L135* loop identified in the molecular dynamics study (24). Fadouloglou et al. have implicated these loops (plus loop *L185*) in active-site accessibility and substrate specificity. Further consideration of proposed ORF BA3524 and BA3888 catalytic functions is presented in a following section.

Enzymatic Characterization of BaBshA and BaBshB

Using a coupled assay, Vetting et al. (16) reported that the dimeric *CgMshA* catalyzes the formation of GlcNAc-Ins-P *via* a sequential (ternary complex) kinetic mechanism in which the donor substrate UDP-GlcNAc almost certainly binds first. The steady-state kinetic parameters determined at pH 7.8, 25°C, yield $K_m(\text{UDP-GlcNAc}) = 0.21 \text{ mM}$, $K_m(\text{Ins-1-P}) = 0.24 \text{ mM}$, and $k_{\text{cat}} = 12.5 \text{ s}^{-1}$. Structural analyses of the apoenzyme and the binary UDP complex demonstrate that nucleotide binding leads to a major rotation of the C-terminal domain relative to the N-terminal domain. $k_{\text{cat}}/K_m(\text{UDP-GlcNAc})$ is $6 \times 10^4 \text{ M}^{-1}\text{s}^{-1}$, and a superposition of the *CgMshA* apoenzyme and UDP complex structures gives an rmsd of ca. 11 Å, underscoring the magnitude of the conformational change in the UDP complex.

Using an HPLC assay for the UDP product, we demonstrated that the *BaBshA* reaction was saturable with respect to both donor and acceptor substrates (Figure 4). At pH 7.5 and 37°C, in the presence of 100 mM NaCl, the apparent kinetic parameters (at 2 mM L-malate) for UDP-GlcNAc are $K_m = 0.37 \text{ mM}$, $k_{\text{cat}} = 28 \text{ s}^{-1}$, and $k_{\text{cat}}/K_m = 7.6 \times 10^4 \text{ M}^{-1}\text{s}^{-1}$. D-Malate, other α -hydroxyacids such as glycolate and D-lactate, and Ins-1-P gave no more than 0.5% of the activity with L-malate when assayed at 0.1 mM (Table S2). The coupled spectrophotometric assay was then employed in an analysis of the steady-state kinetic mechanism for *BaBshA*. As given in Figure S3, the family of reciprocal plots obtained with varying [L-malate] at different fixed [UDP-GlcNAc] intersects below the *x*-axis. This suggests that 1) the kinetic mechanism conforms to a rapid equilibrium random bireactant system (33), as contrasted with an ordered system, and 2) the binding of either substrate to free enzyme increases K^{app} for the second substrate. From the primary plot and secondary *slope* and *intercept* replots, we have determined the kinetic parameters: $K_m(\text{UDP-GlcNAc}) = 0.22 \text{ mM}$, $K_m(\text{L-malate}) = 58 \text{ }\mu\text{M}$, $k_{\text{cat}} = 15 \text{ s}^{-1}$, and $\alpha = 2.6$. $k_{\text{cat}}/K_m(\text{UDP-GlcNAc}) = 6.8 \times 10^4 \text{ M}^{-1}\text{s}^{-1}$, similar to that reported for *CgMshA* at 25°C.

Figure 5 gives a structure-based sequence alignment for *CgMshA* and the three known functional BshA enzymes. An initial description of the *BaBshA* donor substrate binding environment, based on an overlay of the apoenzyme structure with those of the UDP—2-deoxy-2-fluoroglucose complex of the GT4 glucosyltransferase WaaG and the PimA—GDP-mannose complex, identified *BaBshA* His120, Lys211, Glu282, and Glu290 within the active site (14). Figure 5 demonstrates that His120 is conserved in the functional BshA enzymes; the equivalent of this His (His118) is essential for PimA activity (57). Lys211, interacting with the distal phosphate oxygens of UDP, and the two Glu residues, which recognize the sugar 4-OH and the ribose-2'-OH and 3'-OH, respectively, in the PimA complex (57), are conserved in all four sequences. Guerin et al. demonstrated that other residues within the PimA Glu274-Ile278 signature motif, notably Ser275, Phe276, and Ile278, provide main chain hydrogen bonds to the bound mannose sugar moiety, and this motif (*BaBshA* Glu282-Leu286, with Leu replacing Ile) is conserved in the BshA and MshA enzymes. Vetting et al. (16) have identified four *CgMshA* residues (Lys78, Tyr110, Thr134, and Arg154) that coordinate the phosphate of bound Ins-1-P in the ternary complex. As represented in Figure 5, *CgMshA* Tyr110, Thr134, and Arg154 are conserved in all three known functional BshAs, with the single exception of a conservative Arg→Lys substitution in *SaBshA*; *CgMshA* Lys78 is replaced by Val in the sequence alignment. When the

BaBshA apoenzyme is used to query the PDB database with DALI, the closed UDP (and UDP + Ins-1-P complex) structures for *CgMshA* give the highest Z-scores [ca. 37; rmsd = 2.4-2.5 Å (respective A-chains)]. Without adjustments, the superposition represented in Figure 6 gives a clear view of the donor substrate binding environment in *BaBshA*, as described above. In addition, the overlay demonstrates that *CgMshA*-UDP His133 is the structural equivalent of *BaBshA* His120 and identifies *BaBshA* Ile204 (main chain), Asn206, Asp263, and Glu282 as likely recognition elements for the UDP pyrophosphate and for the ribose-2'-OH and uracil oxygens, respectively. There is no evidence for any conformational change on binding of UDP to *BaBshA*, based on the model deduced from this overlay.

The kinetic parameters for *BaBshB* were determined using an HPLC assay for the AccQ-Tag derivative of the GlcN-malate product, as monitored by fluorescence (13,31); Figure 7 gives the resulting initial velocity plot and the fit to the Michaelis-Menten equation. At pH 7.5 and 37°C, in the presence of 50 mM NaCl, the kinetic parameters are $K_m(\text{GlcNAc-malate}) = 0.16 \text{ mM}$, $k_{\text{cat}} = 42 \text{ s}^{-1}$, and $k_{\text{cat}}/K_m(\text{GlcNAc-malate}) = 2.6 \times 10^5 \text{ M}^{-1}\text{s}^{-1}$. We also analyzed the deacetylase activity of *BaBshB* with GlcNAc, at a fixed concentration of 0.15 mM. The observed rate of GlcN production is ca. 10^{-5} that measured with GlcNAc-malate at the same concentration; the L-malate moiety of GlcNAc-malate is therefore a major determinant of substrate recognition and/or transition state stabilization with *BaBshB*. When *BaBshB* was assayed for amidase activity with BSmB (\rightarrow CySmB + GlcN-malate), the observed rate at 0.15 mM substrate is only ca. 2×10^{-5} that for GlcNAc-malate deacetylation.

Structural Analysis of the *BaBshA*-UDP-Malate Complex

In order to test the model for the enzyme-UDP complex described above, and in an attempt to identify the binding determinants for L-malate, we undertook a crystallographic study with the N-terminal His-tagged *BaBshA* protein. This His-tag (MGSH₆SSGLVPRGSHMASMTGGQQMGRGS-) differs from that for the ORF BA1558 construct (MGSSH₆-) analyzed by Ruane et al. (14), which crystallized in space group *P*2₁; there were 12 monomers organized into three tetramers within that asymmetric unit. *BaBshA* crystals belonging to space group *P*4₁ were obtained in 0.2 M Mg(HCO₂)₂ containing 15% PEG3350 with 1 mM each of UDP and L-malate. The structure determined by molecular replacement using the ORF BA1558 apoenzyme coordinates has eight monomers arranged as a dimer of tetramers within the asymmetric unit (Figure 8); gel filtration analysis of the apoenzyme, in the presence of dithiothreitol, suggests that the biological unit for *BaBshA* is the dimer. Refinement at 3.3 Å resolution led to a final model with reasonable statistics (Table 3). The final refined structure is missing the residues of the N-terminal His-tag and Met1, as well as residues 11-13, 42-47, and 60-63; the short internal segments correspond closely to three of the four exposed regions in the final ORF BA1558 model (14). Within the *BaBshA* asymmetric unit, the final model includes two UDP, two malate, and one Mg²⁺ per tetramer; Vetting et al. (16) reported that Ins-1-P soaks of *CgMshA*-UDP crystals resulted in a complex with two UDP, two Mg²⁺, and only one Ins-1-P per dimeric asymmetric unit. The dimeric (substrate-bound) unit of the *BaBshA*-UDP-malate complex gives an overall C_α rmsd of 1.1 Å for 371 atoms when compared with the corresponding dimeric unit of the ORF BA1558 apoenzyme (Figure 9). In addition, the two subunits per tetramer that are complexed with UDP and malate are covalently linked *via* an intersubunit Cys241-Cys241' disulfide (Figure 8); this disulfide is not observed with the complementary unbound subunits within that tetramer, which appear to reflect crystal packing. Focusing on one of the subunits containing bound UDP and malate, Figure 10 gives a final composite omit *F_o-F_c* map in the vicinity of the substrates, together with the refined model. Considering the 3.3 Å resolution of the *BaBshA* complex, we have also

worked with the possibility of modeling glycerol in two conformations as an alternative to malate. Two conformations of glycerol could be modeled into the density; however, after refinement, additional positive density appears. Upon placing malate in the electron density, no additional $F_o - F_c$ density appears.

Bacillithiol is only the second malyl glycoside reported in the literature to date (10,58), and the interactions and specificity determinants for L-malate recognition are of significant interest, particularly given the recent report that L-malate is a second preferred carbon source in *B. subtilis* (59), strongly contributing to repression of the uptake of alternate substrates. An overlay of the CgMshA—UDP-Ins-1-P and BaBshA-UDP-malate complexes (not shown) demonstrates that the positioning and geometry of the Ins-1-P 3-OH and malate 2-OH, relative to the distal phosphates of the respective UDPs, are similar. Neither malate carboxylate is close to the position of the Ins-1-P phosphate, however. Although this interpretation is limited by the 3.3 Å resolution of the BaBshA complex, it is consistent with a chemical mechanism [Scheme 2 (16,60)] involving nucleophilic attack by the malate 2-OH on the anomeric carbon of UDP-GlcNAc.

The superposition of the two complexes also demonstrates that two residues in the CgMshA phosphate coordination site, Tyr110 and Thr134 (see Figure 5), are structurally conserved in BaBshA. BshA Val64 does occupy the same approximate position as MshA Lys78, but the respective Arg138 and Arg154 residues are not equivalent. Figure 11 gives a stereo representation of the BaBshA-UDP-malate active site, focusing on important polar interactions with both malate and UDP. In particular, this analysis identifies Thr122-OH, Asn206-N δ_2 and -O δ_1 , and a distal phosphate oxygen (O1B) of UDP as ligands to the malate C1-carboxylate. The substrate C2-OH interacts with Gly15-N and with both O1B and O2B oxygens of the uridine-pyrophosphate, and Ser16-O stabilizes the C4-carboxylate. All four BaBshA residues are conserved in the other known functional BshA enzymes (Figure 5). It has previously been proposed (61) that an active-site His functions in glycogen phosphorylase and related glycosyltransferases to stabilize an oxocarbenium transition state (e.g., *via* interaction with His377-O in glycogen phosphorylase) such as that considered for CgMshA. This is thought to be especially important for those GT enzymes operating with negatively-charged (e.g., malate, Ins-1-P) acceptor substrates (61), and the conservation of His120 in the BaBshA catalytic center appears to be an important factor in this regard.

With regard to UDP binding, the structure of the BaBshA ternary complex confirms several aspects of the model deduced from the overlay described in Figure 6. The very favorable comparison of apoenzyme and ternary complex structures (Figure 9) demonstrates that there is no major conformational change on substrate binding to BaBshA.

DISCUSSION

BaBshA Structure and Kinetics

In this work we have defined the functions of ORF BA1558, previously annotated as a glycosyltransferase, group 1 family protein, and ORF BA1557, previously annotated as a hypothetical protein, as the *N*-acetyl- α -D-glucosaminyl L-malate synthase (BaBshA) and deacetylase (BaBshB), respectively. The GlcNAc-malate product of BaBshA has been confirmed by ^1H and ^{13}C NMR and by high resolution mass spectrometry; deacetylation by BaBshB gives GlcN-malate, as confirmed by ESP mass spectrometry. The kinetic parameters have been determined for both enzymes. BaBshA is specific for L-malate and does not recognize either D-malate or other α -hydroxyacids as acceptor substrates. BaBshA appears to follow a rapid equilibrium random bireactant mechanism in which the binding of either substrate increases K^{app} for the second substrate (33). Vetting et al. (16) reported that CgMshA followed a sequential mechanism in which UDP-GlcNAc was proposed to bind

first, i.e., as in a rapid equilibrium ordered bireactant scheme. However, Segel has shown that the family of reciprocal plots ($1/v$ versus $1/[\text{Acc}]$, at several fixed $[\text{Don}]$) for such an ordered sequential mechanism intersects on the y -axis, in the case where substrate A (e.g., UDP-GlcNAc) binds first (33). An examination of the data (16) indicates, in contrast, that reciprocal plots of $1/v$ versus $1/[\text{Ins-1-P}]$ for CgMshA intersect in the second quadrant, very close to the x -axis. We suggest that BaBshA and CgMshA both follow rapid equilibrium random bireactant mechanisms; they differ primarily in the fact that $\alpha \sim 1$ for CgMshA. While binding of either substrate to BaBshA has the effect of increasing K^{app} for the second substrate ($\alpha = 2.6$), this interpretation does not apply to CgMshA.

The respective $k_{\text{cat}}/K_{\text{m}}(\text{UDP-GlcNAc})$ values of $6.8 \times 10^4 \text{ M}^{-1}\text{s}^{-1}$ (37°C) and $6 \times 10^4 \text{ M}^{-1}\text{s}^{-1}$ (25°C) correspond to free energies of activation [$\Delta G_{\text{T}}^{\ddagger}$ (62)] of 11.3 kcal/mol and 10.9 kcal/mol. This quantitative similarity is significant, in that Vetting et al. (16) have reported a large conformational change between the CgMshA apoenzyme and UDP complex. Apoenzyme crystals were prepared with an N-terminal His-tagged protein and were of space group $P3_1$, while crystals of the complex were prepared with a C-terminal His-tagged protein and were of space group $I422$. While a crystallographic argument has been presented against the possibility that the apoenzyme conformation does not represent the functional enzyme, this remains an open question. In particular, searches using the CgMshA apoenzyme with the SSM server yielded no significant structural homologs among the GT-B fold family. There is no major conformational change on UDP binding to BaBshA; the possibility of a conformationally distinct BaBshA—UDP-GlcNAc complex also appears unlikely, as the superposition of the BaBshA apoenzyme with the monomeric PimA—GDP-mannose structure reveals similar conformational states ($Z = 33.6$, $\text{rmsd} = 3.0 \text{ \AA}$). In view of the $K_{\text{m}}(\text{UDP-GlcNAc})$ value of 0.22 mM for BaBshA, the intracellular concentration of ca. 2.4 mM reported for *B. megaterium* (63) predicts that ca. 8% of the enzyme is present in the apo form in the *in vivo* steady state. With respect to the BaBshA complex, crystal packing stabilizes a closed tetrameric protein form (two UDP and two malate per tetramer; Figure 8) in which bound UDP is solvent inaccessible. Similarly, Vetting et al. showed that crystals of the dimeric CgMshA-UDP complex, when soaked with high concentrations of UDPGlcNAc, do not exchange bound UDP (16).

Bioinformatics of the *B. anthracis* bsh and pan Operons

Using a transposon site hybridization assay protocol, Day et al. (64) concluded (without the benefit of the functional assignments presented in this work) that the *bshA* and *panC* genes, as well as BA1559 (*pcnB*, Table 1), were individually required for optimal growth, sporulation, or germination in *B. anthracis* strain ΔAmes . As we have demonstrated that deletion of the *bshA* locus in *B. anthracis* Sterne eliminates BSH production, this suggests that BSH is important for one or more of these aspects of the life cycle. In this context, we have recently demonstrated that the *B. subtilis* *bshA* mutant sporulates with an efficiency ca. 1% that of the wild-type strain (13). In their transcriptional profiling of the *B. anthracis* life cycle, in which five distinct temporal waves of gene expression were identified from germination through sporulation, Bergman et al. (65) showed that the *bshA* and *bshB* genes encoding the first two enzymes in the BSH biosynthetic pathway are upregulated together in waves II and III; the *panBCD* genes are upregulated in wave V of the germination→sporulation cycle. *panB* and *panC* are also upregulated between 1 and 2 h postinfection within host macrophages (52).

We have described the gene products for all seven loci in the *bsh* operon, which is upregulated during that part of the life cycle corresponding to early outgrowth → rapid growth (65). Aside from the GlcNAc-malate synthase and deacetylase enzymes, we find no evidence for coding sequences that provide for the enzymatic conversion of GlcN-malate → BSH. In connection with the demonstration that BSH is important for fosfomycin resistance

in *B. anthracis*, the coexpression of the *mgsA* gene encoding methylglyoxal synthase is of interest. Methylglyoxal is cytotoxic in millimolar concentrations and is also mutagenic (51). Still, many bacteria produce methylglyoxal synthase, with a functional implication as a bypass of glycolysis active under conditions of P₁ starvation. In most microorganisms, methylglyoxal is detoxified *via* GSH-dependent conversion to D-lactate; however, we have demonstrated that GSH is absent in *B. anthracis* (2). Both methylglyoxal (51) and fosfomycin (66) are potent C₃-electrophiles known to react with GSH, and our evidence strongly suggests that BSH is the cofactor for FosB in *B. anthracis*. We have recently demonstrated, using a zone of inhibition assay, that a *B. subtilis* *bshA* mutant has a significantly increased sensitivity to methylglyoxal (13). We conclude that BSH may also be the cofactor for an *S*-transferase reaction converting methylglyoxal to lactoylbacillithiol [CH₃CHOHCO-SCH₂CH(NH₃⁺)CO-NGlc-malate]. A possible fate of these BSH conjugates is discussed below.

BaBshB Structure, Function, and Genetics

As indicated previously, BshB is both a structural and functional homolog of *M. tuberculosis* MshB; when assayed in parallel with synthetic GlcNAc-Ins, however, MshB gives k_{cat} of only 0.49 s⁻¹ (31), with $k_{\text{cat}}/K_{\text{m}}(\text{GlcNAc-Ins}) = 1.44 \times 10^3 \text{ M}^{-1}\text{s}^{-1}$. Both values are ca. 1% of the respective parameters with BaBshB (acting on GlcNAc-malate as substrate). The difference in BshB and MshB catalytic efficiencies is approximately that required by rapidly dividing cells to maintain stable levels of BSH or MSH, respectively, given the 50-fold difference in generation times for *B. anthracis* and *M. tuberculosis* (0.5 and 24 h). We have shown that the *B. anthracis* $\Delta bshB$ mutant produces BSH at ca. 70% of the wild-type level, and this has been attributed to an overlapping substrate specificity for two BaBshB paralogs, ORFs BA3524 and BA3888. In the closely related *B. cereus* 14579, the ORF *Bc3461* ortholog of BA3524 has been demonstrated (20) to catalyze deacetylation of both (GlcNAc)₂ and (GlcNAc)₃, and we propose that this enzyme and BcZBP similarly have overlapping specificities for GlcNAc-malate deacetylation in *B. cereus*. A BcZBP-deficient mutant would still be expected to produce significant BSH, through the action of ORF *Bc3461*.

The substrate specificity of the MshB deacetylase overlaps that of the *M. tuberculosis* mycothiol *S*-conjugate amidase (Mca), which functions in the MSH-dependent detoxification of thiol-reactive drugs and metabolites by cleaving the Cys-GlcN amide bond of the *S*-conjugate to give AcCySR plus GlcN-Ins. The optimal amidase substrate for Mca is MSMB, yielding AcCySMB + GlcN-Ins; $k_{\text{cat}}/K_{\text{m}} = 9 \times 10^4 \text{ M}^{-1}\text{s}^{-1}$ at 37°C (23), and MshB catalyzes amide cleavage with this substrate, though with $k_{\text{cat}}/K_{\text{m}} = 460 \text{ M}^{-1}\text{s}^{-1}$ (31), less than 1% of the value observed with Mca. The *M. tuberculosis* Rv1170 mutant deficient in MshB continues to produce MSH at ca. 20% of the wild-type level (67), and this has been attributed to the weak deacetylase activity observed with purified Mca *in vitro* for GlcNAc-Ins [$k_{\text{cat}}/K_{\text{m}} = 0.3 \text{ M}^{-1}\text{s}^{-1}$ (23)], ca. 10⁻⁴ that of MshB (see above). In addition to providing for GlcNAc-malate deacetylation in the absence of BshB (see above), ORFs *Bc3461*, BA3524, and BA3888 may function primarily as paralogs of Mca that catalyze bacillithiol *S*-conjugate amidase reactions related to xenobiotic detoxification. The *S*-conjugates of fosfomycin and methylglyoxal described above represent two potential substrates (Scheme 3). The charged GlcN-malate product of the amidase reaction can be recycled for BSH synthesis, and a number of AcCySR products from the analogous amidase reactions with mycothiol *S*-conjugates are known to be lost from the cell (44,45). Rukmana et al. (68) have recently reported that the Spx regulon is induced in *B. subtilis* cells challenged by the antibiotics enduracin and bacitracin, suggesting that disulfide stress is occurring under these conditions, but the Spx regulatory system appears to be independent of BSH (13).

The Nature and Influence of Low-Molecular-Weight Thiols as Redox Buffers in *B. anthracis*

Bacterial growth and proliferation, especially during infection of the host, often involves a hostile environment (52,53) that challenges the defensive mechanisms of the pathogen (e.g., *B. anthracis* or *S. aureus*). Among the physiological mechanisms for maintaining thiol-disulfide redox homeostasis are the important functions of thiols such as GSH (69,70) and MSH (44,45). *B. anthracis* (2), *S. aureus* (3), and *B. megaterium* (11) are among a number of Gram-positive bacteria that lack both of these thiols. It is clear from several studies, perhaps most closely associated with the Beckwith laboratory (69,70), that redundancy in these systems is the rule, particularly in *E. coli*; mutants lacking either TrxR or glutathione reductase grow normally (70,71).

Figure 12 gives the present working scheme for cytoplasmic disulfide reducing and oxidizing pathways in our model Gram-positive pathogen, *B. anthracis*; the same or very similar system applies in *S. aureus* and in the soil bacterium *B. megaterium*. The three branches include CoASH/CoADR, Trx/TrxR, and bacillithiol (BSH). The recent work of Pöther et al. (12) indicates that cysteine (CySH) represents a fourth branch in *S. aureus*, accounting for most protein (mixed) disulfide formation during diamide stress. While a specific bacillithiol disulfide reductase has not been identified, the BSH/BSSB redox status is very reduced (redox ratio of 84 versus 2.8 for CySH/CySSR) in vegetative *B. anthracis* cells (Table 2); this ratio is unchanged in the Δcdr and $\Delta cdr2$ mutants, and neither CoADR nor CoADR-RHD is a reductant of oxidized bacillithiol (BSSB). There is, however, no direct evidence as to whether the *B. anthracis* Trx/TrxR system might reduce BSSB. In both *Arabidopsis* (72) and *Drosophila* (73), for example, the Trx/TrxR system either constitutes a functional backup or substitutes for glutathione reductase. In *E. coli*, the Grx-SSG reductase activity of AhpC* maintains the reduced GSH pool at essentially wild-type levels in $\Delta gor\Delta trxB$ strains (70).

We recently demonstrated (8) that the *B. anthracis* *cysK-1* locus encoding cysteine synthase A is part of the tricistronic *coaX* operon that also encodes the type III pantothenate kinase. The *B. anthracis* pathway from pantothenate \rightarrow CoASH (Figure 13), as well as the components of the *de novo* pantothenate biosynthetic pathway (including the *panBCD* genes of the *pan* operon; Table 1), have now been established (2,74). In this work we describe the first two steps in BSH biosynthesis for *B. anthracis* and the effects of deleting the respective genes on BSH production. While the identification of the proposed Cys:GlcN-malate ligase, the biological functions of the *B. subtilis* YIIA and ORF BA3524 proteins, and the description of the reductase(s) that maintain the reduced status of BSH in vegetative *B. anthracis* cells remain as priority goals, the materials necessary for genetic analysis of the relative roles of the CoASH/CoADR and BSH systems in both intracellular thiol-disulfide redox homeostasis and in virulence are presently being exploited.

Supplementary Material

Refer to Web version on PubMed Central for supplementary material.

Acknowledgments

We gratefully acknowledge Dr. Robert Fahey, who first identified bacillithiol and led the structure determination, for his generous support and for many very helpful discussions. We thank Dr. Philip Hanna for hosting one of us (C.P.) in his laboratory and contributing to the construction of mutant strains, Dr. James La Clair for help with NMR work, and Ms. Kelly Lo and Mr. Austin Dosch for technical assistance.

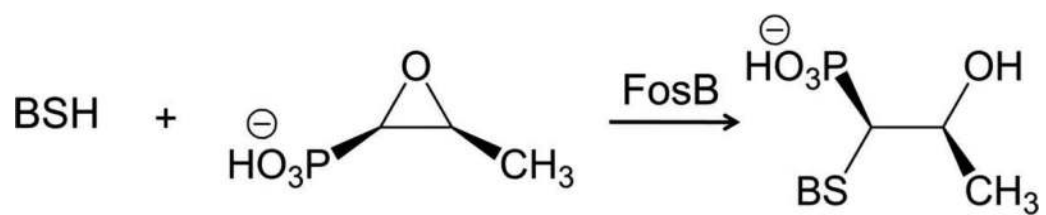
REFERENCES

1. Zuber P. Management of oxidative stress in *Bacillus*. *Annu. Rev. Microbiol.* 2009; 63:575–597. [PubMed: 19575568]
2. Nicely NI, Parsonage D, Paige C, Newton GL, Fahey RC, Leonardi R, Jackowski S, Mallett TC, Claiborne A. Structure of the type III pantothenate kinase from *Bacillus anthracis* at 2.0 Å resolution: implications for coenzyme A-dependent redox biology. *Biochemistry.* 2007; 46:3234–3245. [PubMed: 17323930]
3. delCardayre SB, Stock KP, Newton GL, Fahey RC, Davies JE. Coenzyme A disulfide reductase, the primary low molecular weight disulfide reductase from *Staphylococcus aureus*. Purification and characterization of the native enzyme. *J. Biol. Chem.* 1998; 273:5744–5751. [PubMed: 9488707]
4. Wallen JR, Paige C, Mallett TC, Karplus PA, Claiborne A. Pyridine nucleotide complexes with *Bacillus anthracis* coenzyme A-disulfide reductase: a structural analysis of dual NAD(P)H specificity. *Biochemistry.* 2008; 47:5182–5193. [PubMed: 18399646]
5. delCardayre SB, Davies JE. *Staphylococcus aureus* coenzyme A disulfide reductase, a new subfamily of pyridine nucleotide-disulfide oxidoreductase. Sequence, expression, and analysis of *cdr*. *J. Biol. Chem.* 1998; 273:5752–5757. [PubMed: 9488708]
6. Luba J, Charrier V, Claiborne A. Coenzyme A-disulfide reductase from *Staphylococcus aureus*: evidence for asymmetric behavior on interaction with pyridine nucleotides. *Biochemistry.* 1999; 38:2725–2737. [PubMed: 10052943]
7. Mallett TC, Wallen JR, Karplus PA, Sakai H, Tsukihara T, Claiborne A. Structure of coenzyme A-disulfide reductase from *Staphylococcus aureus* at 1.54 Å resolution. *Biochemistry.* 2006; 45:11278–11289. [PubMed: 16981688]
8. Paige C, Reid SD, Hanna PC, Claiborne A. The type III pantothenate kinase encoded by *coaX* is essential for growth of *Bacillus anthracis*. *J. Bacteriol.* 2008; 190:6271–6275. [PubMed: 18641144]
9. Wallen JR, Mallett TC, Boles W, Parsonage D, Furdui CM, Karplus PA, Claiborne A. Crystal structure and catalytic properties of *Bacillus anthracis* CoADR-RHD: implications for flavin-linked sulfur trafficking. *Biochemistry.* 2009; 48:9650–9667. [PubMed: 19725515]
10. Newton GL, Rawat M, La Clair JJ, Jothivasan VK, Budiarto T, Hamilton CJ, Claiborne A, Helmann JD, Fahey RC. Bacillithiol is an antioxidant thiol produced in *Bacilli*. *Nat. Chem. Biol.* 2009; 5:625–627. [PubMed: 19578333]
11. Swerdlow RD, Setlow P. Purification and characterization of a *Bacillus megaterium* disulfide reductase specific for disulfides containing pantethine 4',4''-diphosphate. *J. Bacteriol.* 1983; 153:475–484. [PubMed: 6401287]
12. Pöther D-C, Liebeke M, Hochgräfe F, Antelmann H, Becher D, Lalk M, Lindequist U, Borovok I, Cohen G, Aharonowitz Y, Hecker M. Diamide triggers mainly S-thiolations in the cytoplasmic proteomes of *Bacillus subtilis* and *Staphylococcus aureus*. *J. Bacteriol.* 2009; 191:7520–7530. [PubMed: 19837798]
13. Gaballa A, Newton GL, Antelmann H, Parsonage D, Upton H, Rawat M, Claiborne A, Fahey RC, Helmann JD. Biosynthesis and functions of bacillithiol, a major low-molecular-weight thiol in *Bacilli*. *Proc. Natl. Acad. Sci. USA.* 2010; 107:6482–6486. [PubMed: 20308541]
14. Ruane KM, Davies GJ, Martinez-Fleites C. Crystal structure of a family GT4 glycosyltransferase from *Bacillus anthracis* ORF BA1558. *Proteins.* 2008; 73:784–787. [PubMed: 18712829]
15. Newton GL, Ta P, Bzymek KP, Fahey RC. Biochemistry of the initial steps of mycothiol biosynthesis. *J. Biol. Chem.* 2006; 281:33910–33920. [PubMed: 16940050]
16. Vetting MW, Frantom PA, Blanchard JS. Structural and enzymatic analysis of MshA from *Corynebacterium glutamicum*: substrate-assisted catalysis. *J. Biol. Chem.* 2008; 283:15834–15844. [PubMed: 18390549]
17. Franco OL, Rigden DJ. Fold recognition analysis of glycosyltransferase families: further members of structural superfamilies. *Glycobiology.* 2003; 13:707–712. [PubMed: 12881407]
18. Cantarel BL, Coutinho PM, Rancurel C, Bernard T, Lombard V, Henrissat B. The Carbohydrate-Active enZymes database (CAZy): an expert resource for glycogenomics. *Nucleic Acids Res.* 2009; 37:D233–238. [PubMed: 18838391]

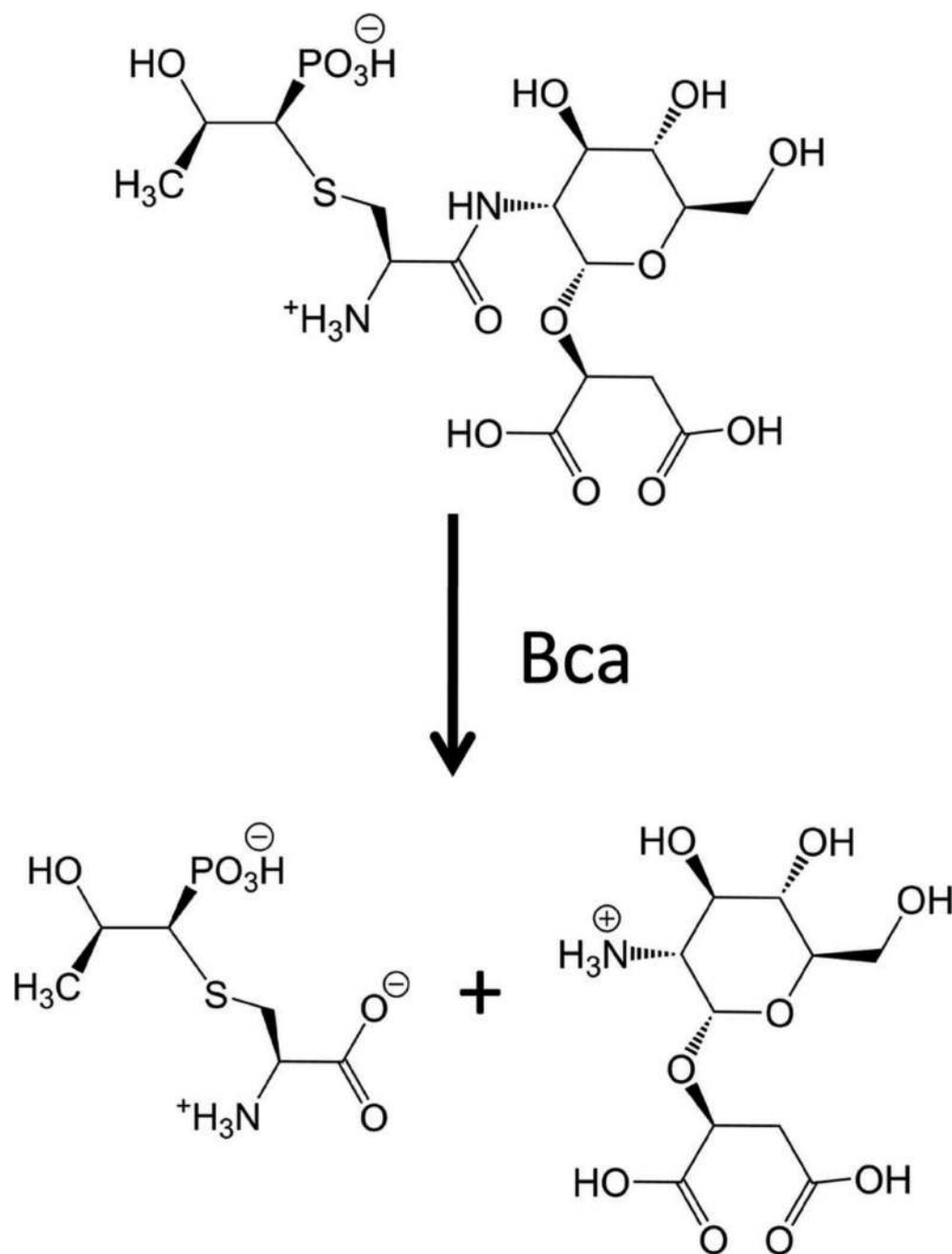
19. Fadouloglou VE, Deli A, Glykos NM, Psylinakis E, Bouriotis V, Kokkinidis M. Crystal structure of the BcZBP, a zinc-binding protein from *Bacillus cereus*. FEBS J. 2007; 274:3044–3054. [PubMed: 17501983]
20. Deli A, Koutsoulidis D, Fadouloglou VE, Spiliotopoulou P, Balomenou S, Arnaouteli S, Tzanodaskalaki M, Mavromatis K, Kokkinidis M, Bouriotis V. LmbE proteins from *Bacillus cereus* are de-N-acetylases with broad substrate specificity and are highly similar to proteins in *Bacillus anthracis*. FEBS J. 2010; 277:2740–2753. [PubMed: 20491912]
21. Watanabe R, Ohishi K, Maeda Y, Nakamura N, Kinoshita T. Mammalian PIG-L and its yeast homologue Gpi12p are N-acetylglucosaminylphosphatidylinositol de-N-acetylases essential in glycosylphosphatidylinositol biosynthesis. Biochem J. 1999; 339:185–192. [PubMed: 10085243]
22. Maynes JT, Garen C, Cherney MM, Newton GL, Arad D, Av-Gay Y, Fahey RC, James MNG. The crystal structure of 1-D-*myo*-inosityl 2-acetamido-2-deoxy- α -D-glucopyranoside deacetylase (MshB) from *Mycobacterium tuberculosis* reveals a zinc hydrolase with a lactate dehydrogenase fold. J. Biol. Chem. 2003; 278:47166–47170. [PubMed: 12958317]
23. Steffek M, Newton GL, Av-Gay Y, Fahey RC. Characterization of *Mycobacterium tuberculosis* mycothiol S-conjugate amidase. Biochemistry. 2003; 42:12067–12076. [PubMed: 14556638]
24. Fadouloglou VE, Stavrakoudis A, Bouriotis V, Kokkinidis M, Glykos NM. Molecular dynamics simulations of BcZBP, a deacetylase from *Bacillus cereus*: active site loops determine substrate accessibility and specificity. J. Chem. Theory Comput. 2009; 5:3299–3311.
25. Kim HU, Goepfert JM. A sporulation medium for *Bacillus anthracis*. J. Appl. Bacteriol. 1974; 37:265–267. [PubMed: 4212901]
26. Fisher N, Hanna P. Characterization of *Bacillus anthracis* germinant receptors *in vitro*. J. Bacteriol. 2005; 187:8055–8062. [PubMed: 16291679]
27. Janes BK, Stibitz S. Routine markerless gene replacement in *Bacillus anthracis*. Infect. Immun. 2006; 74:1949–1953. [PubMed: 16495572]
28. Ouyang SP, Sun SY, Liu Q, Chen J, Chen GQ. Microbial transformation of benzene to *cis*-3,5-cyclohexadien-1,2-diols by recombinant bacteria harboring toluene dioxygenase gene *tod*. Appl. Microbiol. Biotechnol. 2007; 74:43–49. [PubMed: 17021870]
29. McLaughlin RE, Ferretti JJ. Electrotransformation of streptococci. Methods Mol. Biol. 1995; 47:185–193. [PubMed: 7550734]
30. Studier FW. Protein production by auto-induction in high density shaking cultures. Protein Expr. Purif. 2005; 41:207–234. [PubMed: 15915565]
31. Newton GL, Ko M, Ta P, Av-Gay Y, Fahey RC. Purification and characterization of *Mycobacterium tuberculosis* 1D-*myo*-inosityl-2-acetamido-2-deoxy- α -D-glucopyranoside deacetylase, MshB, a mycothiol biosynthetic enzyme. Protein Expr. Purif. 2006; 47:542–550. [PubMed: 16630724]
32. Calendar R, Berg P. The catalytic properties of tyrosyl ribonucleic acid synthetases from *Escherichia coli* and *Bacillus subtilis*. Biochemistry. 1966; 5:1690–1695. [PubMed: 4289778]
33. Segel, IH. Enzyme Kinetics. John Wiley & Sons; New York: 1975.
34. Gosselin S, Alhussaini M, Streiff MB, Takabayashi K, Palcic MM. A continuous spectrophotometric assay for glycosyltransferases. Anal. Biochem. 1994; 220:92–97. [PubMed: 7978262]
35. Anderberg SJ, Newton GL, Fahey RC. Mycothiol biosynthesis and metabolism. J. Biol. Chem. 1998; 273:30391–30397. [PubMed: 9804803]
36. Otwinowski Z, Minor W. Processing of X-ray diffraction data collected in oscillation mode. Methods Enzymol. 1997; 276:307–326.
37. McCoy AJ, Grosse-Kunstleve RW, Adams PD, Winn MD, Storoni LC, Read RJ. *Phaser* crystallographic software. J. Appl. Cryst. 2007; 40:658–674. [PubMed: 19461840]
38. Adams PD, Afonine PV, Bunkoczi G, Chen VB, Davis IW, Echols N, Headd JJ, Hung LW, Kapral GJ, Grosse-Kunstleve RW, McCoy AJ, Moriarty NW, Oeffner R, Read RJ, Richardson DC, Richardson JS, Terwilliger TC, Zwart PH. *PHENIX*: a comprehensive Python-based system for macromolecular structure solution. Acta Cryst. 2010; D66:213–221.
39. Emsley P, Cowtan K. Coot: model-building tools for molecular graphics. Acta Crystallogr. 2004; D60:2126–2132.

40. Holm L, Park J. DaliLite workbench for protein structure comparison. *Bioinformatics*. 2000; 16:566–567. [PubMed: 10980157]
41. DeLano, WL. The PyMOL Molecular Graphics System. DeLano Scientific; San Carlos, CA: 2002.
42. Thompson JD, Higgins DG, Gibson TJ. CLUSTAL W: improving the sensitivity of progressive multiple sequence alignment through sequence weighting, position-specific gap penalties and weight matrix choice. *Nucleic Acids Res*. 1994; 22:4673–4680. [PubMed: 7984417]
43. Gouet P, Courcelle E, Stuart DI, Metoz F. ESPript: analysis of multiple sequence alignments in PostScript. *Bioinformatics*. 1999; 15:305–308. [PubMed: 10320398]
44. Newton GL, Buchmeier N, Fahey RC. Biosynthesis and functions of mycothiol, the unique protective thiol of *Actinobacteria*. *Microbiol. Mol. Biol. Rev*. 2008; 72:471–494. [PubMed: 18772286]
45. Jothivasan VK, Hamilton CJ. Mycothiol: synthesis, biosynthesis and biological functions of the major low molecular weight thiol in actinomycetes. *Nat. Prod. Rep*. 2008; 25:1091–1117. [PubMed: 19030604]
46. Sareen D, Steffek M, Newton GL, Fahey RC. ATP-dependent L-cysteine:1D-*myo*-inosityl 2-amino-2-deoxy- α -D-glucopyranoside ligase, mycothiol biosynthesis enzyme MshC, is related to class I cysteinyl-tRNA synthetases. *Biochemistry*. 2002; 41:6885–6890. [PubMed: 12033919]
47. Newberry KJ, Hou YM, Perona JJ. Structural origins of amino acid selection without editing by cysteinyl-tRNA synthetase. *EMBO J*. 2002; 21:2778–2787. [PubMed: 12032090]
48. Passalacqua KD, Varadarajan A, Ondov BD, Okou DT, Zwick ME, Bergman NH. The structure and complexity of a bacterial transcriptome. *J. Bacteriol*. 2009; 191:3203–3211. [PubMed: 19304856]
49. Bergman NH, Passalacqua KD, Hanna PC, Qin ZS. Operon prediction for sequenced bacterial genomes without experimental information. *Appl. Environ. Microbiol*. 2007; 73:846–854. [PubMed: 17122389]
50. Lobley CM, Schmitzberger F, Kilkenny ML, Whitney H, Ottenhof HH, Chakauya E, Webb ME, Birch LM, Tuck KL, Abell C, Smith AG, Blundell TL. Structural insights into the evolution of the pantothenate-biosynthesis pathway. *Biochem Soc. Trans*. 2003; 31:563–571. [PubMed: 12773157]
51. Saadat D, Harrison DH. The crystal structure of methylglyoxal synthase from *Escherichia coli*. *Structure*. 1999; 7:309–317. [PubMed: 10368300]
52. Bergman NH, Anderson EC, Swenson EE, Janes BK, Fisher N, Niemeyer MM, Miyoshi AD, Hanna PC. Transcriptional profiling of *Bacillus anthracis* during infection of host macrophages. *Infect. Immun*. 2007; 75:3434–3444. [PubMed: 17470545]
53. Passalacqua KD, Bergman NH, Lee JY, Sherman DH, Hanna PC. The global transcriptional responses of *Bacillus anthracis* Sterne (34F2) and a Δ *sodA1* mutant to paraquat reveal metal ion homeostasis imbalances during endogenous superoxide stress. *J. Bacteriol*. 2007; 189:3996–4013. [PubMed: 17384197]
54. Fuchs, G. Biosynthesis of building blocks. In: Schlegel, HG., editor. *Biology of the Prokaryotes*. Blackwell Science, Inc.; Malden, MA: 1999. p. 110-160.
55. Krepinsky K, Leimkühler S. Site-directed mutagenesis of the active site loop of the rhodanese-like domain of the human molybdopterin synthase sulfurase MOCS3. Major differences in substrate specificity between eukaryotic and bacterial homologs. *FEBS J*. 2007; 274:2778–2787. [PubMed: 17459099]
56. Cao M, Bernat BA, Wang Z, Armstrong RN, Helmann JD. FosB, a cysteine-dependent fosfomycin resistance protein under the control of σ^W , an extracytoplasmic-function σ factor in *Bacillus subtilis*. *J. Bacteriol*. 2001; 183:2380–2383. [PubMed: 11244082]
57. Guerin ME, Kordulakova J, Schaeffer F, Svetlikova Z, Buschiazzi A, Giganti D, Gicquel B, Mikusova K, Jackson M, Alzari PM. Molecular recognition and interfacial catalysis by the essential phosphatidylinositol mannosyltransferase PimA from mycobacteria. *J. Biol. Chem*. 2007; 282:20705–20714. [PubMed: 17510062]
58. Rotzoll N, Dunkel A, Hofmann T. Activity-guided identification of (*S*)-malic acid 1-*O*-D-glucopyranoside (morelid) and γ -aminobutyric acid as contributors to umami taste and mouth-drying oral sensation of morel mushrooms (*Morchella deliciosa* Fr.). *J. Agric. Food Chem*. 2005; 53:4149–4156. [PubMed: 15884853]

59. Kleijn RJ, Buescher JM, Le Chat L, Jules M, Aymerich S, Sauer U. Metabolic fluxes during strong carbon catabolite repression by malate in *Bacillus subtilis*. *J. Biol. Chem.* 2010; 285:1587–1596. [PubMed: 19917605]
60. Errey JC, Lee SS, Gibson RP, Martinez-Fleites C, Barry CS, Jung PM, O'Sullivan AC, Davis BG, Davies GJ. Mechanistic insight into enzymatic glycosyl transfer with retention of configuration through analysis of glycomimetic inhibitors. *Angew. Chem. Int. Ed.* 2010; 49:1234–1237.
61. Mitchell EP, Withers SG, Ermert P, Vasella AT, Garman EF, Oikonomakos NG, Johnson LN. Ternary complex crystal structures of glycogen phosphorylase with the transition state analogue nojirimycin tetrazole and phosphate in the T and R states. *Biochemistry.* 1996; 35:7341–7355. [PubMed: 8652510]
62. Fersht, A. *Structure and Mechanism in Protein Science*. W.H. Freeman and Company; New York: 1999.
63. Mengin-Lecreux D, Allen NE, Hobbs JN, van Heijenoort J. Inhibition of peptidoglycan biosynthesis in *Bacillus megaterium* by daptomycin. *FEMS Microbiol. Lett.* 1990; 57:245–248. [PubMed: 2170230]
64. Day WA Jr, Rasmussen SL, Carpenter BM, Peterson SN, Friedlander AM. Microarray analysis of transposon insertion mutations in *Bacillus anthracis*: global identification of genes required for sporulation and germination. *J. Bacteriol.* 2007; 189:3296–3301. [PubMed: 17277068]
65. Bergman NH, Anderson EC, Swenson EE, Niemeyer MM, Miyoshi AD, Hanna PC. Transcriptional profiling of the *Bacillus anthracis* life cycle *in vitro* and an implied model for regulation of spore formation. *J. Bacteriol.* 2006; 188:6092–6100. [PubMed: 16923876]
66. Brown DW, Schaab MR, Birmingham WR, Armstrong RN. Evolution of the antibiotic resistance protein, FosA, is linked to a catalytically promiscuous progenitor. *Biochemistry.* 2009; 48:1847–1849. [PubMed: 19196010]
67. Buchmeier NA, Newton GL, Koledin T, Fahey RC. Association of mycothiol with protection of *Mycobacterium tuberculosis* from toxic oxidants and antibiotics. *Mol. Microbiol.* 2003; 47:1723–1732. [PubMed: 12622824]
68. Rukmana A, Morimoto T, Takahashi H, Giyanto, Ogasawara N. Assessment of transcriptional responses of *Bacillus subtilis* cells to the antibiotic duracidin, which interferes with cell wall synthesis, using a high-density tiling chip. *Genes Genet. Syst.* 2009; 84:253–267. [PubMed: 20057163]
69. Ortenberg RB, Beckwith J. Functions of thiol-disulfide oxidoreductases in *E. coli*: redox myths, realities, and practicalities. *Antioxid. Redox Signal.* 2003; 5:403–411. [PubMed: 13678528]
70. Faulkner MJ, Veeravalli K, Gon S, Georgiou G, Beckwith J. Functional plasticity of a peroxidase allows evolution of diverse disulfide-reducing pathways. *Proc. Natl. Acad. Sci. USA.* 2008; 105:6735–6740. [PubMed: 18456836]
71. Prinz WA, Åslund F, Holmgren A, Beckwith J. The role of the thioredoxin and glutaredoxin pathways in reducing protein disulfide bonds in the *Escherichia coli* cytoplasm. *J. Biol. Chem.* 1997; 272:15661–15667. [PubMed: 9188456]
72. Marty L, Siala W, Schwarzländer M, Fricker MD, Wirtz M, Sweetlove LJ, Meyer Y, Meyer AJ, Reichheld J-P, Hell R. The NADPH-dependent thioredoxin system constitutes a functional backup for cytosolic glutathione reductase in *Arabidopsis*. *Proc. Natl. Acad. Sci. USA.* 2009; 106:9109–9114. [PubMed: 19451637]
73. Kanzok SM, Fechner A, Bauer H, Ulschmid JK, Müller HM, Botella-Munoz J, Schneuwly S, Schirmer R, Becker K. Substitution of the thioredoxin system for glutathione reductase in *Drosophila melanogaster*. *Science.* 2001; 291:643–646. [PubMed: 11158675]
74. Gerdes SY, Scholle MD, D'Souza M, Bernal A, Baev MV, Farrell M, Kurnasov OV, Daugherty MD, Mseeh F, Polanuyer BM, Campbell JW, Anantha S, Shatalin KY, Chowdhury SA, Fonstein MY, Osterman AL. From genetic footprinting to antimicrobial drug targets: examples in cofactor biosynthetic pathways. *J. Bacteriol.* 2002; 184:4555–4572. [PubMed: 12142426]

**Scheme 1.**

Catalytic addition of bacillithiol (BSH) to fosfomycin, as proposed for FosB.

**Scheme 3.**

Bacillithiol *S*-conjugate amidase (Bca) reaction proposed for ORFs *Bc3461*, *BA3524*, and *BA3888*. The *S*-conjugate of fosfomycin (Scheme 1) is taken as the substrate.

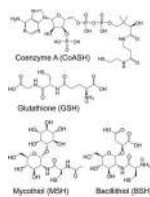


Figure 1.
Low-molecular-weight thiol redox buffers.



Figure 2. Mycothiol biosynthetic pathway (upper), and proposed bacillithiol biosynthetic pathway (lower).



Figure 3. Structure-based sequence alignment for *BcZBP*, *BaBshB*, and ORFs BA3888, BA3524, and *Bc3461*. Secondary structure assignments correspond to *BcZBP*; red boxes represent conserved residues, and yellow boxes represent conservative substitutions. Active-site loops *L*₄₆, *L*₁₃₅, and *L*₁₈₅ as defined for *BcZBP* (24) are indicated, as are the insert *I1* and deletions *D1* and *D2* described in the text. Green and blue triangles represent ligands to the *BcZBP* active-site Zn²⁺ and the proposed acid-base catalyst (Asp14) and charge-relay dyad (His110/Asp112), respectively.

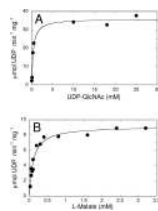


Figure 4. (A) UDP-GlcNAc dependence for *BaBshA* with 2 mM L-malate. (B) L-Malate dependence with 3 mM UDP-GlcNAc.

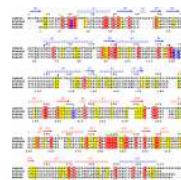


Figure 5. Structure-based sequence alignment for *CgMshA* and the three known functional BshAs. Secondary structure assignments (color-coded by domain) correspond to the *CgMshA*—UDP-Ins-1-P complex. BshA sequences correspond to *B. subtilis* [*BsuBshA* (YpjH, Ref 13)], *S. aureus* JH9 (YP_001246887), and *B. anthracis*. *CgMshA* and *BaBshA* residue numbering are shown above and below the alignment, respectively. Green and blue triangles denote residues from *CgMshA* that interact with the modeled UDP-GlcNAc substrate and with the phosphate of Ins-1-P, respectively. Blue boxes represent active-site residues conserved in BshA and thought to be important for L-malate binding and catalysis. Other details are as in Figure 3.

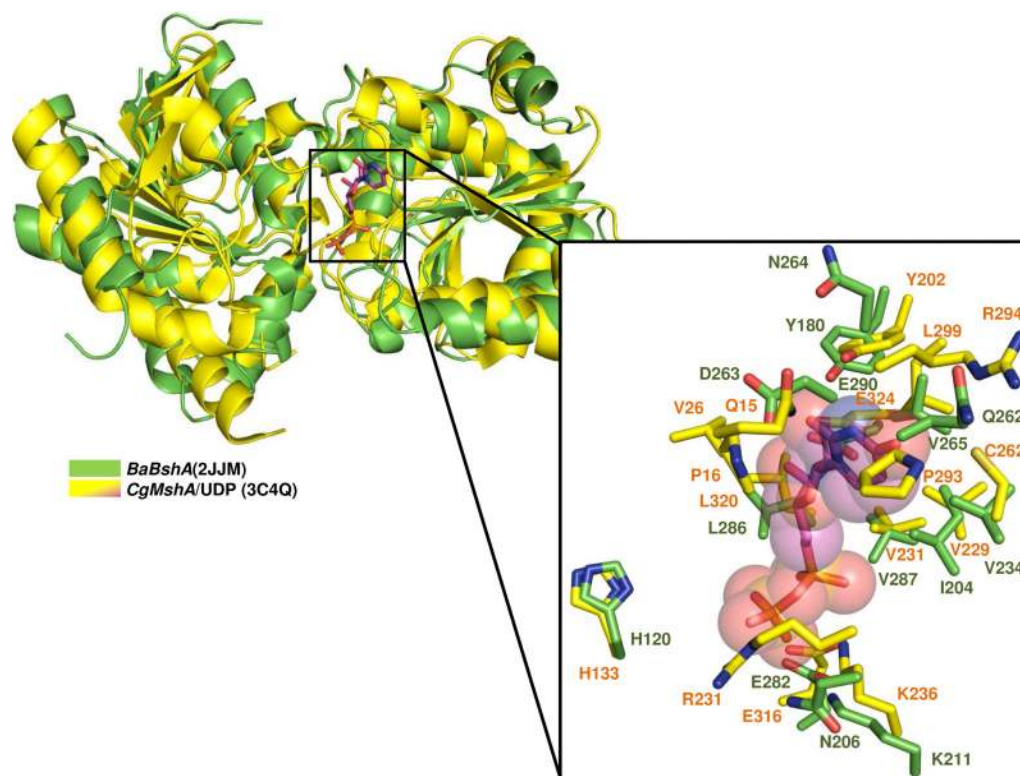


Figure 6. Monomer (left) and active-site (right) overlay for the ORF BA1558 apoenzyme and the *CgMshA*-UDP complex. The superposition was performed using PyMOL with the respective A-chains for PDB entries 2JJM (ORF BA1558) and 3C4Q (*CgMshA*-UDP), as described in the text. ORF BA1558 and *CgMshA* side chains (stick diagram) are color-coded by atom type, with carbon atoms colored green and yellow, respectively. Bound UDP (*CgMshA*, with space-filling overlay rendered as 50% transparent) is included and is color-coded by atom type, with carbon atoms colored magenta. Active-site overlay depicts the bound UDP and all residues within 4 Å, as well as the *BaBshA* His120/*CgMshA* His133 pair.

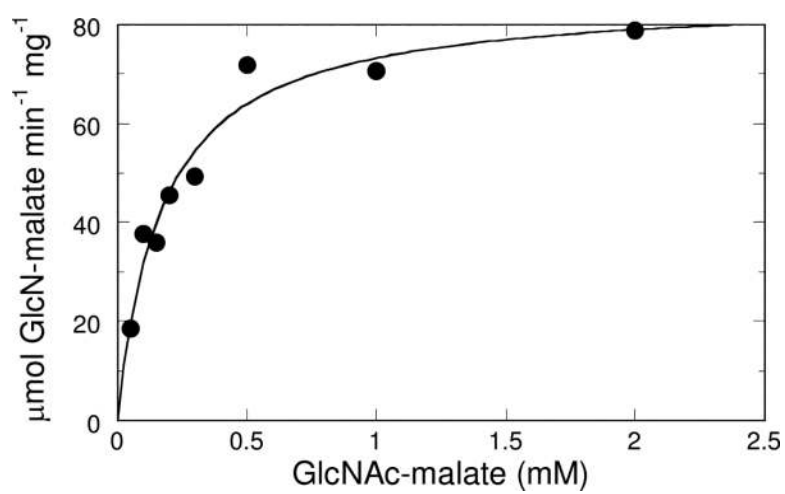


Figure 7.
GlcNAc-malate dependence for *BaBshB*.

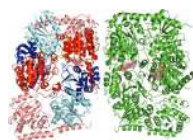


Figure 8.

Asymmetric unit for the *BaBshA* ternary complex. The asymmetric unit consists of a dimer of tetramers; the polypeptides of one tetramer (left) are color-coded by domains. The two polypeptides that do not contain bound substrate (cyan, N-terminal domain; salmon, C-terminal domain) are distinguished from the substrate-bound monomers (blue, N-terminal domain; red, C-terminal domain). The substrate-bound monomers are linked by the Cys241-Cys241' disulfide (yellow). The second tetramer (right) within the asymmetric unit is colored green. For both tetramers, bound UDP molecules are color-coded as in Figure 6, malate is color-coded by atom type, with carbon atoms colored blue, and magnesium ions in the respective active sites (one per substrate-bound dimer) are colored red. Stereoviews of the *BaBshA* ternary complex, focusing on important active-site interactions, are given in Figures 10 and 11.

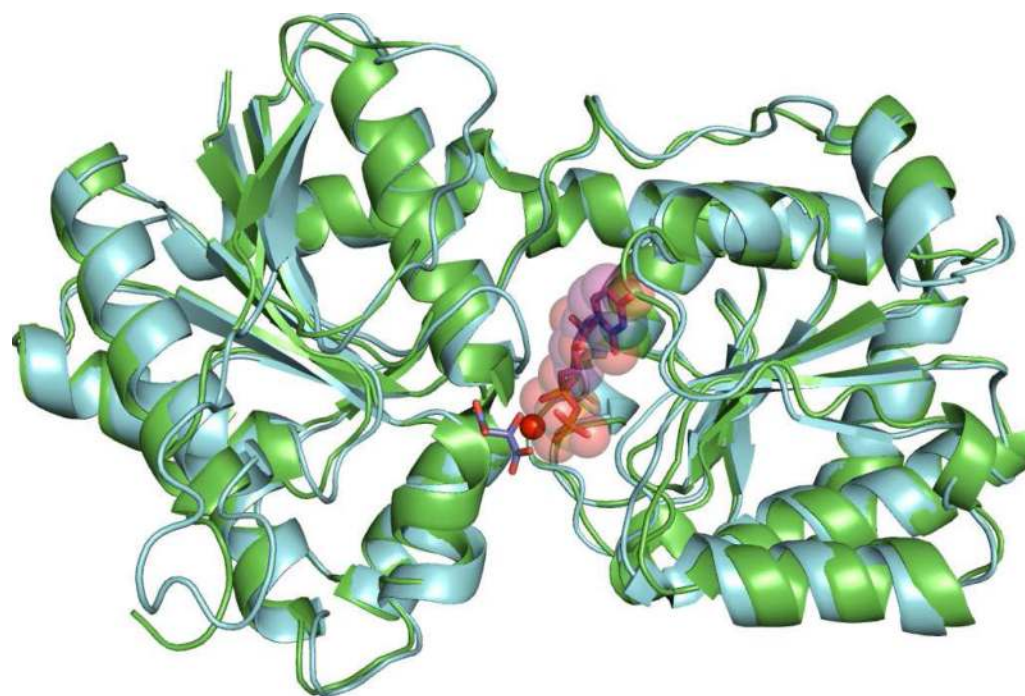


Figure 9. Superposition of the *BaBshA*-UDP-malate complex (chain A, cyan) with an apoenzyme (PDB entry 2JJM) monomer (green). An overlay with the respective dimers gives rmsd = 1.1 Å for 371 C_α atoms. Bound UDP, malate, and magnesium ion are color-coded as in Figure 8.

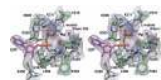


Figure 10.

Stereoview of the *BaBshA*-UDP-malate complex, focusing on the active site. The refined model includes bound UDP and malate, Mg^{2+} , one water molecule (Water 295), and protein segments corresponding to His120, Ser205-Asn206, Val210-Lys211, Glu282-Val287, and Glu290. A composite omit F_o-F_c map is shown contoured at 1.2σ . All atoms are color-coded as in Figure 8 except for *BaBshA* C_α and side chain carbon atoms, which are colored green.

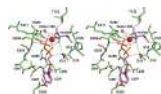


Figure 11. Stereo representation of the *BaBshA* ternary complex, focusing on important polar interactions with UDP and malate. Hydrogen-bonding interactions, shown as black dotted lines, are shown for bound UDP, malate, Mg²⁺, and Water 295. All atoms are color-coded as in Figure 10.

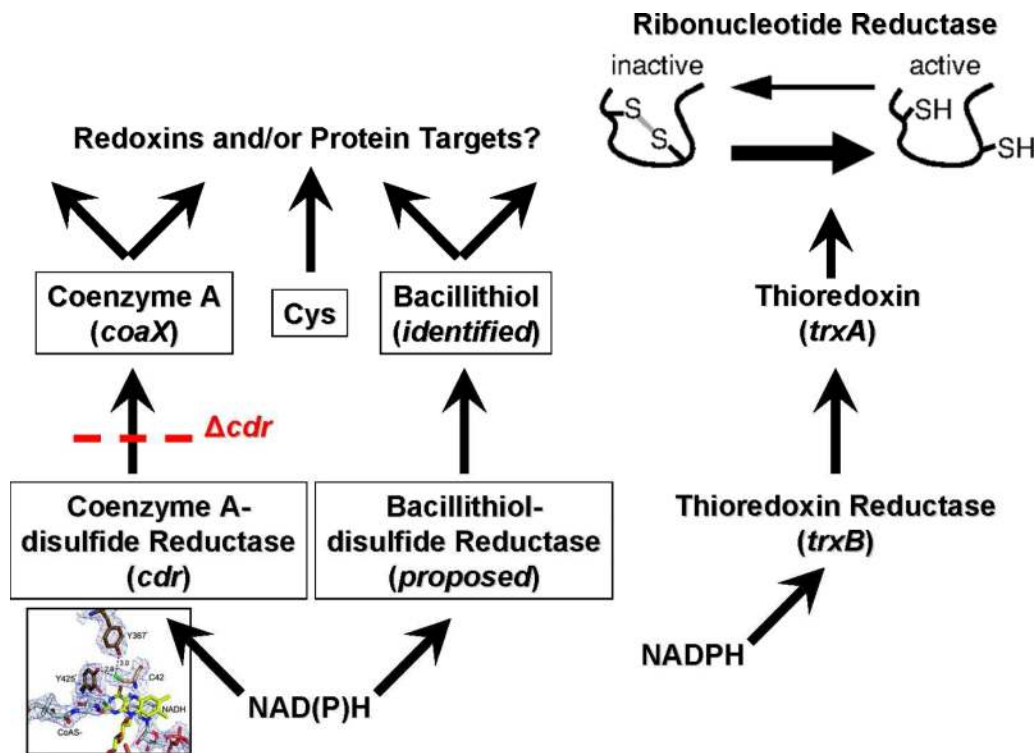


Figure 12.

Cytoplasmic thiol redox pathways in *B. anthracis*. Structural genes are identified in parentheses beneath the respective proteins; the *coaX* gene encodes the type III pantothenate kinase that catalyzes the first step in CoASH biosynthesis. Results with the Δcdr mutant are described in Table 2 and in the text. TrxA appears to reduce ribonucleotide reductase in *B. subtilis*, but this is still under investigation. The thumbnail representation of the *B. anthracis* CoADR active-site structure is adapted from Figure 5 of Ref 4.

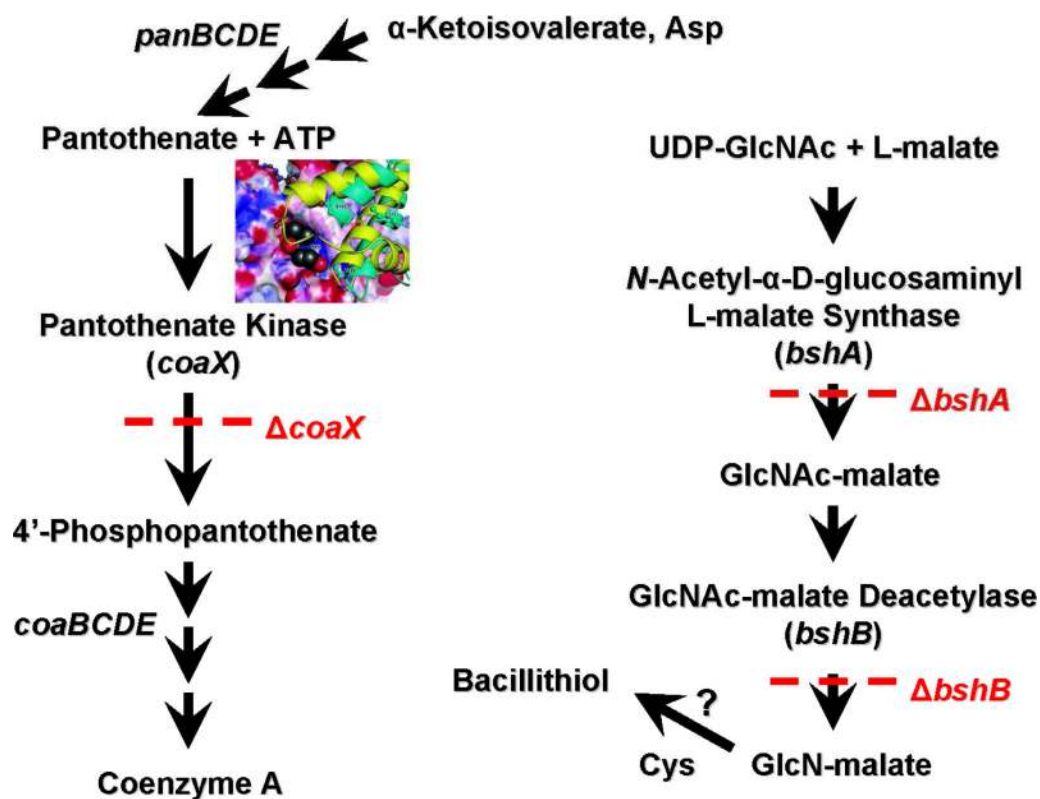


Figure 13.

CoASH and BSH biosynthetic pathways in *B. anthracis*. Structural genes are identified in parentheses beneath the respective proteins; the properties of the $\Delta bshA$ and $\Delta bshB$ mutants are described in Table 2 and in the text. The properties of a conditional *coaX* mutant have been reported (8). The thumbnail representation of the *B. anthracis* pantothenate kinase active-site structure is adapted from Figure 7 of Ref 2.

Table 1Bioinformatics of the *B. anthracis* *bsh* and *pan* Operons

Gene	Functional homolog/PDB entry ^a	Comparison
BA1554	Putative pyrophosphatase YpjD/2GTA (<i>B. subtilis</i>)	74% identity; <i>E</i> value 4e ⁻⁴⁵
BA1555 (<i>dapB</i>)	Dihydrodipicolinate reductase/1YL6 (<i>M. tuberculosis</i>)	44% identity; <i>E</i> value 3e ⁻⁴⁸
BA1556 (<i>mgsA</i>)	Methylglyoxal synthase/1B93 (<i>E. coli</i>)	50% identity; <i>E</i> value 2e ⁻³²
BA1557 (<i>bshB</i>)	GlcNAc-malate deacetylase/2IXD (<i>B. cereus</i>)	96% identity; <i>E</i> value 6e ⁻¹³³
BA1558 (<i>bshA</i>)	GlcNAc-malate synthase/2IJM	identical
BA1559 (<i>pcnB</i>)	tRNA CCA-adding enzyme/1MIY (<i>Bacillus stearothermophilus</i>)	49% identity; <i>E</i> value 4e ⁻¹⁰⁶
BA1560 (<i>birA</i>)	Biotin:CoASAc carboxylase ligase/1WNL (<i>Pyrococcus horikoshii</i>)	32% identity; <i>E</i> value 7e ⁻³⁶
BA1562 (<i>panB</i>)	Ketopantoate hydroxymethyltransferase/1M3U (<i>E. coli</i>)	46% identity; <i>E</i> value 1e ⁻⁶³
BA1563 (<i>panC</i>)	Pantothenate synthetase/2X3F (<i>S. aureus</i>)	53% identity; <i>E</i> value 2e ⁻⁸⁷
BA1564 (<i>panD</i>)	Aspartate decarboxylase proenzyme/2C45 (<i>M. tuberculosis</i>)	55% identity; <i>E</i> value 1e ⁻³³
BA1565	Putative PolC-type DNA polymerase III, exonuclease domain/2P1J (<i>Thermotoga maritima</i>)	34% identity; <i>E</i> value 1e ⁻¹⁶

^aObtained with BLASTP using the PDB proteins database.

Table 2

Low-Molecular-Weight Thiol Contents and Redox Ratios for *B. anthracis* Sterne Wild-Type and Mutant Strains

Strain	Thiol and Disulfide Contents ($\mu\text{mol per g dry weight}^a$) and Redox Ratios ^b									
	BSH	BSSR/0.5	Redox ratio	CySH	CySSR/0.5	Redox ratio	CoASH ^c	S=SO ₃ ²⁻		
Wild-type	1.1 \pm 0.1	0.027 \pm 0.004	84	0.40 \pm 0.04	0.29 \pm 0.04	2.8	1.9 \pm 0.4	2.2 \pm 0.4		
Δ <i>bshA</i>	<0.03	<0.002	—	0.22 \pm 0.06	0.43 \pm 0.09	1.0	1.8 \pm 0.4	2.0 \pm 0.4		
Δ <i>bshB</i>	0.79 \pm 0.02	0.013 \pm 0.002	122	0.39 \pm 0.02	0.47 \pm 0.056	1.7	3.0 \pm 0.7	2.4 \pm 0.4		
Δ <i>cdr</i>	0.95 \pm 0.12	0.022 \pm 0.003	86	0.39 \pm 0.04	0.43 \pm 0.054	1.8	1.4 \pm 0.3	2.2 \pm 0.2		
Δ <i>cdr2</i>	1.2 \pm 0.06	0.03 \pm 0.01	80	0.41 \pm 0.02	0.40 \pm 0.12	2.1	1.6 \pm 0.3	2.2 \pm 0.2		
Δ <i>cdr</i> Δ <i>cdr2</i>	0.88 \pm 0.03	0.015 \pm 0.002	118	0.46 \pm 0.02	0.28 \pm 0.02	3.2	1.8 \pm 0.1	2.5 \pm 0.3		

^aMean of triplicate determinations (10).^bExpressed as thiol/disulfide (RSH/RSSR), where disulfide is estimated as half the thiol content released by dithiothreitol from an *N*-ethylmaleimide-blocked sample (10).^cIncludes 3'-dephospho-CoASH; redox ratio cannot be determined with confidence due to contribution from cleavage of acyl-CoAs by the dithiothreitol reagent (2,10).

Table 3Data Collection^a and Refinement Statistics for the *BaBshA*

Complex with UDP and Malate	
	<i>BaBshA</i> -UDP-malate
Data collection	
Space group	$P4_1$
Cell dimensions	
a, b, c (Å)	226.3, 226.3, 75.4
α, β, γ (°)	90, 90, 90
Wavelength (Å)	1.000
Resolution (Å)	226-3.31 (3.39-3.31) ^b
I/σ	12.3 (1.3)
Completeness (%)	99.2 (93.9)
Redundancy	5.7 (2.7)
Refinement statistics	
Resolution (Å)	226-3.31
No. reflections	54419
R_{work}	0.229
R_{free}	0.259
Molecules per asymmetric unit (AU)	8
No. of amino acid residues per AU	2961
No. of waters per AU	288
Average <i>B</i> -factors	69.7
Stereochemical ideality	
Bond length rmsd (Å)	0.009
Bond angle rmsd (°)	1.97
Φ, ψ preferred (%)	93.7
Φ, ψ allowed (%)	5.90
Φ, ψ outliers (%)	0.40
PDB entry	3MBO

^aCollected at SER-CAT beamline BM-22 of the Advanced Photon Source.^bNumbers in parentheses represent data for the highest resolution shell.